In-situ Photoemission Spectroscopy Characterization of Electronic States in Semiconductor Interfaces

by

Xingye Wang

A Dissertation Presented in Partial Fulfillment
of the Requirements for the Degree
Doctor of Philosophy

Approved April 2018 by the
Graduate Supervisory Committee:

Robert Nemanich, Chair
Candace Chan
Fernando Ponce
Zachary Holman

ARIZONA STATE UNIVERSITY

May 2018

ABSTRACT

The electronic states of semiconductor interfaces have significant importance for semiconductor device performance, especially due to the continuing miniaturization of device technology.

The application of ultra high vacuum (UHV) enables the preparation and characterization of fresh and cleaned interfaces. In a UHV environment, photoemission spectroscopy (PES) provides a non-destructive method to measure the electronic band structure, which is a crucial component of interface properties.

In this dissertation, three semiconductor interfaces were studies to understand different effects on electronic states. The interfaces studied were freshly grown or pre-treated under UHV. Then *in-situ* PES measurements, including x-ray photoemission spectroscopy (XPS) and ultra-violet photoemission spectroscopy (UPS), were conducted to obtain electronic states information.

First, the CdTe/InSb (100) heterointerface was employed as a model interface for II-VI and III-V heterojunctions. It was suggested that an interface layer formed, which consisted of In-Te bonding. The non-octal bonding between In and Te atoms has donor-like behavior, which was proposed to result in an electron accumulation layer in InSb. A type-I heterointerface was observed. Second, Cu/ZnO interfaces were studied to understand the interface bonding and the role of polarization on ZnO interfaces. It was shown that on O-face ZnO (0001) and PEALD ZnO, copper contacts had ohmic behavior. However, on Zn-face ZnO (0001), a 0.3 eV Schottky barrier height was observed. The lower than expected barrier heights were attributed to oxygen vacancies introduced by Cu-O bonding during interface formation. In addition, it is suggested that the different barrier

heights on two sides of ZnO (0001) are caused by the different behavior for the ZnO (0001) faces. Last, a pulse mode deposition method was applied for P-doped diamond growth on (100) diamond surfaces. Pretreatment effects were studied. It is suggested that an O/H plasma treatment or a short period of H-plasma and CH_4/H_2 plasma could yield a higher growth rate. PES measurements were conducted on H-terminated intrinsic diamond surface and P-doped/intrinsic diamond (100) interfaces. It was suggested that electronic states near the valence band maximum caused Fermi level pinning effects, independent of the diamond doping.

DEDICATION

This dissertation is dedicated to my wife, my parents and my family.

ACKNOWLEDGMENTS

First, I would like to express my gratitude to my Ph.D. and master's advisor, Regent Professor Robert J. Nemanich. It is my pleasure to work with him and in the NanoScience Lab. It would be impossible for me to finish this up without his tremendous support and help during my graduate study. In addition, his knowledge and enthusiasm for materials science and physics always inspire me. This experience will undoubtedly benefit me in the years to come.

I greatly appreciate the assistance of my committee members: Dr. Candace Chan, Dr. Fernando Ponce and Dr. Zachary Holman. The suggestions to the development of this work are important to me. In addition, I appreciate them for serving as my committee. Especially, I want to acknowledge Dr. Fernando Ponce's help during my study. The materials physics courses were the one of the first courses I took at ASU, and the contents are widely used in my researches.

This research is financially supported by the National Science Foundation under Grant #DMR-1206935 and Microwave Enterprise, Ltd.

I want to express my appreciation to Franz Koeck. His help and support during my Ph.D. period are meaningful to me. The experience and attitude I got from working with him will be very beneficial for me.

It was delightful experience to work with the amazing people at ASU. I would like to appreciate Dr. Tianyin Sun, Dr. Jialing Yang and Dr. Manpuneet Benipal for their patient and detailed advices at the beginning of my research. I would like to extend my appreciation to Yu Yang for the collaboration and useful discussions. I would also like to thank Dr. Fu Tang, Dr. Chiyu Zhu and Dr. Xin Liu for sharing the experience and

knowledge on instruments with me. I am glad to extend the acknowledgement to Dr. Brianna Eller, Dr. Joe Shammas, Dr. Anna Zanewski, Aaron Papagalos, Mei Hao, Yichen Yao, Daniel Messina, Jesse Brown, Dr. Qian Cheng and Dr. Qianlang Liu.

It has been my pleasure to work with Dr. John Venables and Dr. Ernst Bauer. Their enthusiasm for science and knowledge always amazes me. Besides, the suggestions in my projects are helpful.

I would also like to thank the people working in the SEMTE program, Physics program and Leroy Eyring Center for Solid State Science, who have always been helpful and supportive.

Last, I would like to thank my wife, my parents, my other family members and my friends for their love and supports that I have received for years.

TABLE OF CONTENTS

Page

CHAPTER Page

CHAPTER Page

CHAPTER Page

LIST OF TABLES

Table Page

LIST OF FIGURES

Figure Page

Figure Page

CHAPTER 1

INTRODUCTION

1.1 Introduction

As Herbert Kroemer pointed out during his speech for the 2000 Nobel Prize in Physics, “By increasing miniaturization in semiconductor-device technology, the interface itself is the device.” [1]. Semiconductor interfaces usually have significantly different properties from those of the bulk materials. Interfaces combine different electronic states from materials, which provides interesting phenomena and another degree of freedom for manipulating the design of devices.

However, the electronic states at semiconductor interfaces, which determine device behavior, are extremely difficult to predict, and could be affected by intrinsic electronic states such as interface and surface states and extrinsic electronic states introduced by defects and chemical bonding. Consequently, factors from the material choices to interface preparation methods could affect the interface electronic states. As a result, a method for electronic states characterization becomes critical to understand a realistic interface. *In-situ* photoemission spectroscopy (PES) provides an effective method for electronic states measurement at interfaces [2], and the employment of UHV technology enables a clean environment for interface preparation and characterization.

1.2 Electronic states in semiconductor interfaces

1.2.1 Semiconductor surfaces states

The surface can be considered as a particularly simple type of interface between solid and vacuum or atmosphere [3]. Because it is the termination of a bulk material, the bonds between bulk atoms are not repeated for the surfaces atoms. Thus, additional energy is required for surface formation. There are two major differences between surfaces and bulk materials: first, for semiconductor surfaces, the translational symmetry is only valid in the direction within the plane of surfaces. In the vertical direction to the surface, the period properties no longer exist close to the surface. This can lead to new electronic levels at the surface. In addition, because of the different atom bonds at the surfaces, the configuration of the surface atoms may change from the crystalline structure of the bulk materials. Surface relaxations and reconstructions are common at semiconductor surfaces, which normally causes the electronic states to vary at the surfaces too. The uncertainty of atomic position further increases the difficulty of a calculation of the electronic structure at surfaces. Because of these two major differences, the surface electronic structures are significantly different from bulk.

For ideal, clean surfaces, electronic states can be related to the nearly-free-electron approximation or the tight bonding approximation [4-6]. There is no physical distinction between these two approaches. In the tight bonding picture, for the surface atoms, the bonding partners are missing from one side, which results in less overlap of the wavefunction with neighborhood atoms. Thus, the split and shift in energy level from atom to crystal is weaker as shown in FIG. 1.1. These separated states (Tamm states) from the bulk conduction band and the valence band are surface states. Atomic orbitals, which are involved in chemical bonding, provide surface levels when perturbated by the surface. For example, the sp^3 bonds in diamond become dangling bonds at a surface. This effect

provides dangling bond surface states, which are significantly different from states in the bulk material. Besides, surface states can also be affected by back bonds, which are related to the chemical bonding close to the surface layers [7].

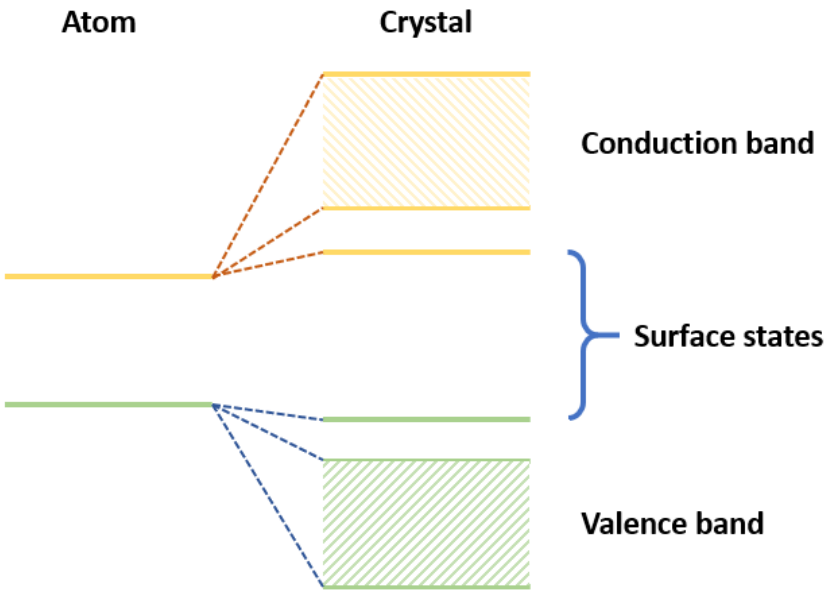

FIG. 1.1. A schematic of the origin of surface states from the tight bonding approach.

In addition to the intrinsic surface states mentioned above, extrinsic surface states, which are related to imperfections, are also commonly observed at realistic semiconductor surfaces.

1.2.2 Metal-Induced Gap States and Virtual-Induced Gap States

Like semiconductor surfaces, the solid/solid interfaces are complicated too. An oversimplified model for metal/semiconductor interfaces is shown in FIG. 1.2. An n-type semiconductor material and a large work function metal are used in this example.

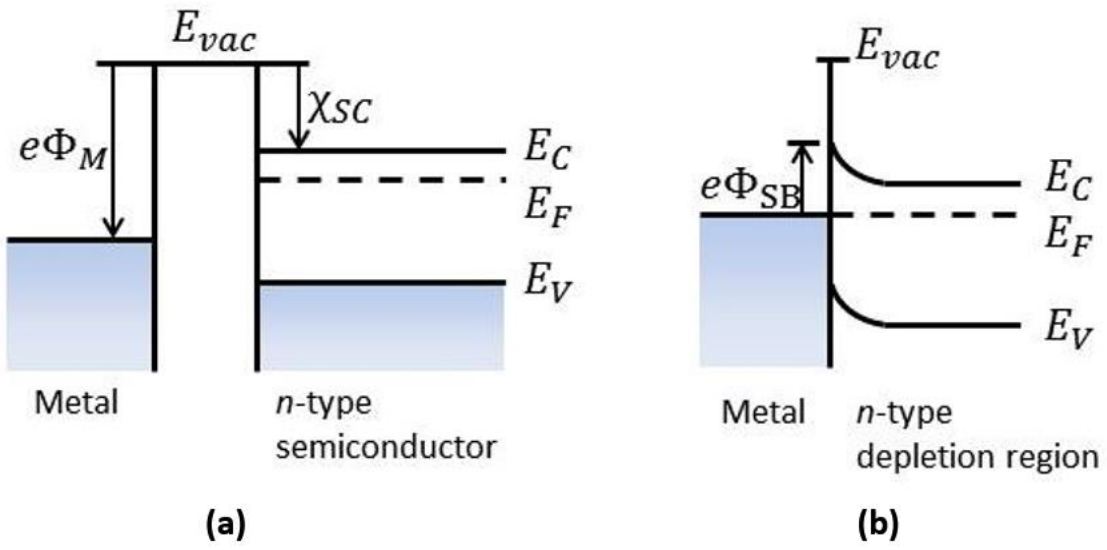

FIG. 1.2. Illustration of metal/n-type semiconductor interface formation.

In addition to the match between the metal work function and the electron affinity of the semiconductor, the Fermi level of metal needs to align with the semiconductor material because of thermal equilibrium. Thus, charge transfer occurs at the interface. In a metal, the charge is screened within a few Å. However, the depletion region in a semiconductor material can extend beyond a few hundred Å, because of the significantly lower density of free carriers in the semiconductor. Band bending occurs in the semiconductor accordingly. However, this model is oversimplified. For a realistic metal/semiconductor interface, chemical bonding between the deposited metal and semiconductor material could cause charge transfer at the interface, which changes the electronic states of the original semiconductor. Moreover, alloy formation and atom inter-diffusion can introduce new interface states.

Fermi level pinning is a common characteristic of metal/semiconductor interface, which can be caused by Metal-induced gap states (MIGS) [8-10]. When the metal contacts with semiconductor, the Bloch wavefunction tails into the semiconductor regime [11]. The

conduction band of the metal overlaps with the band gap of semiconductor, which introduces new interface states into semiconductor. Virtual gap states (VIGS) are similar to MIGS, but for a semiconductor heterojunction, where the electronic states from one semiconductor could tail into the band gap of the other semiconductor and consequently cause interface states.

1.2.3 Chemistry- and Structure-Dependent Models of Interface States

Besides the VIGS and MIGS, chemical bonding and crystal structure changes can also result in changes interface states. Here, non-octal bonding and oxygen vacancies in zinc oxide are used for illustration of these interface states.

Non-octal chemical bonding plays an important role at heterovalent heterointerfaces. In a stable tetrahedrally bonded material, each bond contains two electrons [12]. For example, in a zincblende structure semiconductor, GaAs, each Ga atom provides 3 electrons and As atom provides 5 electrons. Since there are 4 bonds for each atom, on average, there are two electrons in each bond. However, at heterovalent interfaces, such as IV/IIV-V or II-VI/III-V interfaces, non-octal bonding will occur between II-V, III-VI, IV-IIV and IV-V atoms, which results in an average of 7/4 or 9/4 electrons per bond instead of 2 electrons. These bonds provide a deficit or excess of 1/4 electron and act as acceptors or donors respectively, causing charge transfer at the interface region and consequently leading to the loss of local charge neutrality. Thus, band alignment would be further affected. The effects would be the strongest when an abrupt interface with only one kind of non-octal bonding occurs, which could provide a charge density of $> 10^{14}$ charges/cm^2. Although Harrison *et al.* theoretically suggested the necessity of atomic

mixing at these interfaces because of the electrical field build up [13], the unbalance between donor-like and acceptor-like non-octal bonding is not uncommon [14, 15]. Thus, direct measurements of electronic states for heterovalent interface states are important.

Intentional introduction of impurities has been applied to modify the electronic states in semiconductors for decades. Besides intentional introduction of impurities, other point defects, including vacancies, interstitials and antisites, could also contribute to changing the electronic states. Generally, native defects counteract with predominant dopants. However, the native defects in zinc oxide are believed to influence the electrical properties more significantly, including causing unintentional n-type conductivity [16]. Oxygen vacancies and zinc interstitials are often considered as the most likely sources of the n-type conductivity. Although the oxygen vacancy behaves like a donor and has the lowest formation energy among the donor-like native point defects, calculation results have shown that the donor level is rather deep, which makes it difficult to be ionized [17, 18]. However, recent experimental research indicated that oxygen vacancies are +2 charged even close to the conduction band minimum (CBM) and proposed that oxygen vacancies are the dominant donor-like native point defects for ZnO n-type behavior [19]. Although the debate on the origin of the zinc oxide n-type conductivity continues, the electronic states effects induced by defects are more evident.

1.3 Dissertation approach

With the extensive growth in the semiconductor industry, semiconductor interfaces become critical for device design and fabrication. However, different electronic states at

interfaces from bulk materials may be unavoidable during device fabrication. Thus, understanding these interfaces is necessary.

Since these effects occur at surfaces and can be affected by contaminants in air, measurements in a UHV environment are critical to understand the intrinsic properties. In this dissertation, the research focuses on *in-situ* characterization of electronic states of interfaces using photoemission spectroscopy technique. A VG Scienta photoemission spectroscopy system including a MX650 monochromatic aluminum x-ray source, a UV40 UV source from Prevac and a R3000 hemispherical high-resolution electron energy analyzer was first built and optimized. I led the development of this PES system, which is now being used on multiple projects involving all the graduate students in the Nanoscience Laboratory.

In Chapter 2, the instruments and analysis methods used in the studies are explained. The introduced equipments include: photoemission spectroscopy systems, atomic layer deposition systems and chemical vapor deposition systems. Moreover, a series of characterization methods based on photoemission spectroscopy measurements are described.

In Chapter 3, the electronic states of the CdTe/InSb (100) heterojunction are studied as a model heterojunction of II-VI and III-V semiconductors. The CdTe/InSb (100) heterojunctions have attracted considerable attention because of its almost perfect lattice match and the potential for non-octal interface bonding. Because of the polar character of the interface, the number of II-V and III-VI bonds could be unbalanced, which leads to excess and deficit electrons from non-octal bonding and charge (electron or hole) accumulation. Photoemission spectroscopy was applied in this study to determine the band

alignment at the heterointerface. It was indicated that a 1.5 nm thick interface layer with In-Te bonds was formed at the interface. The bonds have donor-like behavior and cause electron accumulation at the InSb side of the interface, which further resulted in a 0.2 eV downward band bending. A valence band offset of 0.89 eV was measured and a type-I heterojunction band alignment was obtained.

In Chapter 4, the band alignment at Cu/ZnO interfaces were studied. Zinc oxide is a promising wide bandgap semiconductor because of its properties such as high mobility, and direct band gap. Wurtzite zinc oxide shows polar behavior in the (0001) direction. According to x-ray diffraction (XRD) measurement, plasma-enhanced atomic layer deposition (PEALD) zinc oxide film may provide decreased polar properties. A fundamental understanding of metal/ZnO interfaces with respect to the different properties of ZnO (0001) and $(000\bar{1})$ surfaces is necessary. Since the work function of copper (4.6 eV) is just slightly higher than the electron affinity of zinc oxide (χ=4.0~4.3 eV), potentially, the face differences could affect the copper/ZnO interface behavior. Photoemission spectroscopy was applied in this study and a change between ohmic and Schottky behavior was indicated. It was proposed that the oxygen vacancies at the interfaces caused the lower Schottky barriers than expected. In addition, the different properties of ZnO faces affected the oxygen vacancy density, which can lead to different contact behaviors.

In Chapter 5, the electronic states of the interfaces of phosphorus-doped diamond deposited on intrinsic diamond (100) were studied with photoemission spectroscopy. Diamond is an ultra-wide bandgap semiconductor attracting extensive attention for high temperature, high power and high frequency applications. Phosphorus is considered as a promising candidate n-type dopant. However, the phosphorus incorporation on diamond

(100) surface is still a challenge. In this study, we achieved epitaxial growth of P-doped diamond on intrinsic diamond (100) by employing a pulse mode deposition method. A preferred pretreatment process was established. It is suggested that a low surface roughness is important for a high growth rate and efficient dopant incorporation for phosphorus-doped diamond on (100) surfaces. Photoemission spectroscopy was used to determine the electronic states and band alignment of the H-terminated P-doped diamond/i-diamond interface. The diamond (100) Fermi levels were pinned in a small range near the valence band maximum independent to its doping. It is attributed to the diamond surface states and air-exposure induced states.

Chapter 6 summarizes the studies in this dissertation, and an outline of future studies is presented.

References:

1. *The Nobel Prize in Physics 2000*. 2000; Available from: http://www.nobelprize.org/nobel_prizes/physics/laureates/2000/.

2. Franciosi, A. and C.G. Van de Walle, *Heterojunction band offset engineering.* Surface Science Reports, 1996. **25**(1-4): p. 1-140.

3. Lüth, H., *Solid surfaces, interfaces and thin films*. 4th, rev. and extended ed. 2001, Berlin ; New York: Springer. xiii, 559 p.

4. Forstmann, F., *The concepts of surface states.* Progress in Surface Science, 1993. **42**(1-4): p. 21-31.

5. Shockley, W., *On the Surface States Associated with a Periodic Potential.* Physical Review, 1939. **56**(4): p. 317-323.

6. Tamm, I., *On the possible bound states of electrons on a crystal surface.* Phys. Z. Soviet Union, 1932(1): p. 733.

7. Müller, G., A. Friedberger, and K. Knese, *Porous Silicon Based MEMS.* 2015: p. 503-524.

8. Mönch, W., *Barrier heights of real Schottky contacts explained by metal-induced gap states and lateral inhomogeneities.* Journal of Vacuum Science & Technology B: Microelectronics and Nanometer Structures, 1999. **17**(4): p. 1867.

9. Nishimura, T., K. Kita, and A. Toriumi, *Evidence for strong Fermi-level pinning due to metal-induced gap states at metal/germanium interface.* Applied Physics Letters, 2007. **91**(12): p. 123123.

10. Tejedor, C., F. Flores, and E. Louis, *The metal-semiconductor interface: Si (111) and zincblende (110) junctions.* Journal of Physics C: Solid State Physics, 1977. **10**(12): p. 2163-2177.

11. Heine, V., *Theory of Surface States.* Physical Review, 1965. **138**(6A): p. A1689-A1696.

12. Farrell, H.H., M.C. Tamargo, J.L. de Miguel, F.S. Turco, D.M. Hwang, and R.E. Nahory, *"Designer" interfaces in II-VI/III-V polar heteroepitaxy.* Journal of Applied Physics, 1991. **69**(10): p. 7021-7028.

13. Harrison, W.A., E.A. Kraut, J.R. Waldrop, and R.W. Grant, *Polar heterojunction interfaces.* Physical Review B, 1978. **18**(8): p. 4402-4410.

14. Xi, S., W. Jie, G. Zha, Y. Yuan, T. Wang, W. Zhang, J. Zhu, L. Xu, Y. Xu, J. Su, H. Zhang, Y. Gu, J. Li, J. Ren, and Q. Zhao, *Effects of Ga-Te interface layer on the*

potential barrier height of CdTe/GaAs heterointerface. Phys. Chem. Chem. Phys., 2016. **18**(4): p. 2639-2645.

15. Frey, A., U. Bass, S. Mahapatra, C. Schumacher, J. Geurts, and K. Brunner, *Band offsets and band bending at heterovalent semiconductor interfaces.* Physical Review B, 2010. **82**(19).

16. Janotti, A. and C.G. Van de Walle, *Fundamentals of zinc oxide as a semiconductor*. Reports on Progress in Physics, 2009. **72**(12): p. 126501.

17. Janotti, A. and C.G. Van de Walle, *New insights into the role of native point defects in ZnO*. Journal of Crystal Growth, 2006. **287**(1): p. 58-65.

18. Janotti, A. and C.G. Van de Walle, *Oxygen vacancies in ZnO*. Applied Physics Letters, 2005. **87**(12): p. 122102.

19. Liu, L., Z. Mei, A. Tang, A. Azarov, A. Kuznetsov, Q.-K. Xue, and X. Du, *Oxygen vacancies: The origin of n-type conductivity in ZnO*. Physical Review B, 2016. **93**(23).

CHAPTER 2

INSTRUMENTS AND ANALYSIS METHOD

2.1 Introduction

In-situ experiments in this dissertation were mainly accomplished in the NanoScience Lab (NSL) using the integrated ultra-high vacuum (UHV) system. This integrated UHV system consists of nine sample processing and growth chambers, six characterization chambers, a sample storage box, and a ~20 m transfer line, which connects the fifteen chambers, is pumped by five cryogenic pumps and operates at a base pressure of $\sim 5 \times 10^{-10}$ Torr. Each chamber is separated from the transfer line with a gate valve, which are closed during normal operation. Two loadlock systems are located at the two ends of the transfer line for loading samples. A cart with three sample positions, which is driven by a manual crank, is used for transferring the sample between the chambers. The processing and growth systems include: a reactive molecular electron beam deposition system (MBD) for metal oxide film deposition, an electron cyclotron resonance microwave plasma chemical vapor deposition (ECR MPCVD) system for BN film growth, a remote plasma enhanced atomic layer deposition (PEALD) system for fluoride film deposition, an atomic layer etching (ALE) system, a remote plasma system for plasma cleaning and etching, another remote PEALD system for oxide film deposition, a low energy electron diffraction (LEED) system for crystal structure analysis, a molecular beam epitaxy (MBE) system for GaN deposition, an electron beam physical vapor deposition (EBPVD) system for metal film deposition, an integrated photoemission spectroscopy (PES) system, which consists of a monochromatic x-ray photoemission spectroscopy (XPS) for core-level and

stoichiometry characterizations and an ultra-violet photoemission spectroscopy (UPS) for valence band and work function analysis, a UV spectrometer system for UV reflectivity and/or transmission measurements, another XPS system, an Auger electron spectroscopy (AES) system, another UPS system and a sputtering system. A schematic and a picture of the NSL UHV system are shown in FIG. 2.1.

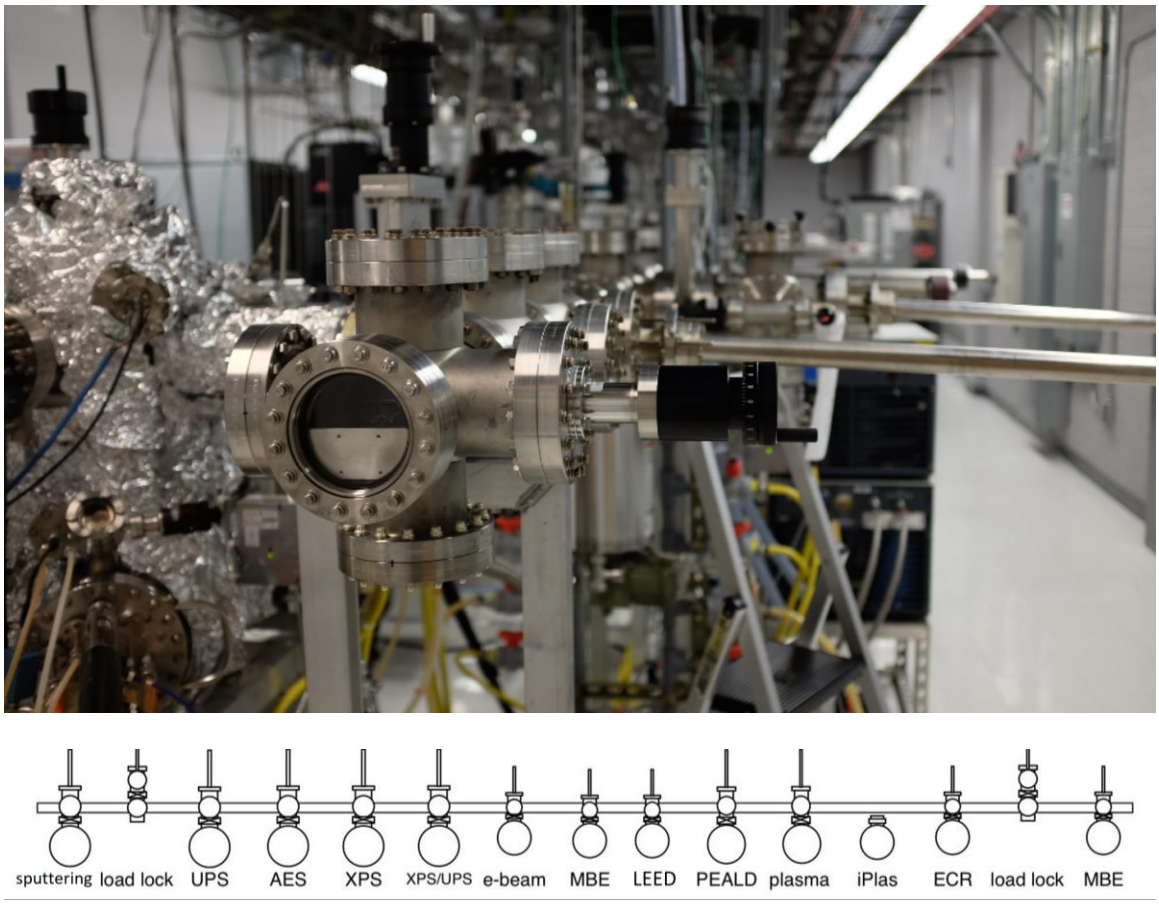

FIG. 2.1. A view and a schematic of the integrated NSL UHV system.

The *ex-situ* facilities and equipment employed for the research in this dissertation include: two microwave plasma enhanced chemical vapor deposition (MPCVD) systems for diamond sample pretreatment and phosphorus-doped diamond film growth, a dual-chamber molecular beam epitaxy system for II-VI and III-V growth, two chemical rooms

for sample *ex-situ* cleaning and preparation, a prototype Elmitec LEEM III instrument for mirror electron microscopy and low energy electron microscopy measurement, an Asylum research MFP-3D classic atomic force microscopy and a differential interference contrast (DIC) microscopy for surface morphology characterization.

2.2 Photoemission Spectroscopy

2.2.1 Principle of Photoemission Spectroscopy

Photoemission spectroscopy is a powerful tool that enables measurement of the electronic states at semiconductor interfaces [1]. The system, which is in an ultra-high vacuum environment, consists of a light source, electron optics, an electron analyzer and an electron detector. The universal curve shown in FIG. 2.2 illustrates the mean free path of electrons versus electron kinetic energy [2]. Data indicate that compared to other technologies using atoms or ions for surface spectroscopy, electrons carry information on only the outermost few angstroms to nanometers, which means that PES is suited to probe electronic states at the surface or near surface region [3]. A three-step model, presented in FIG. 2.3, is commonly used to describe the mechanism of photoemission spectroscopy. In the three-step model, the photoemission process is divided into three distinct processes: first, photoexcitation excites electrons within a range of micrometers depth, from a bound state to an empty state. Then the excited electrons transport to the surface. Finally, electrons with sufficient energy overcome the surface energy barrier, and are emitted into vacuum and contribute to the spectrum. The emitted electrons are then collected and dispersed by an electron spectrometer. However, in the second step, according to the universal curve, the electrons that are deep in the sample are mostly scattered to lower energy states that do

not relate to the initial state. Some scattered electrons still have sufficient energy to overcome the surface energy barrier. They are emitted as secondary electrons and form a background in the spectrum, which increases in intensity close to the low energy threshold. Since the energy and momentum of these electrons are changed by scattering events, they cannot be considered directly related to the initial electron bound state.

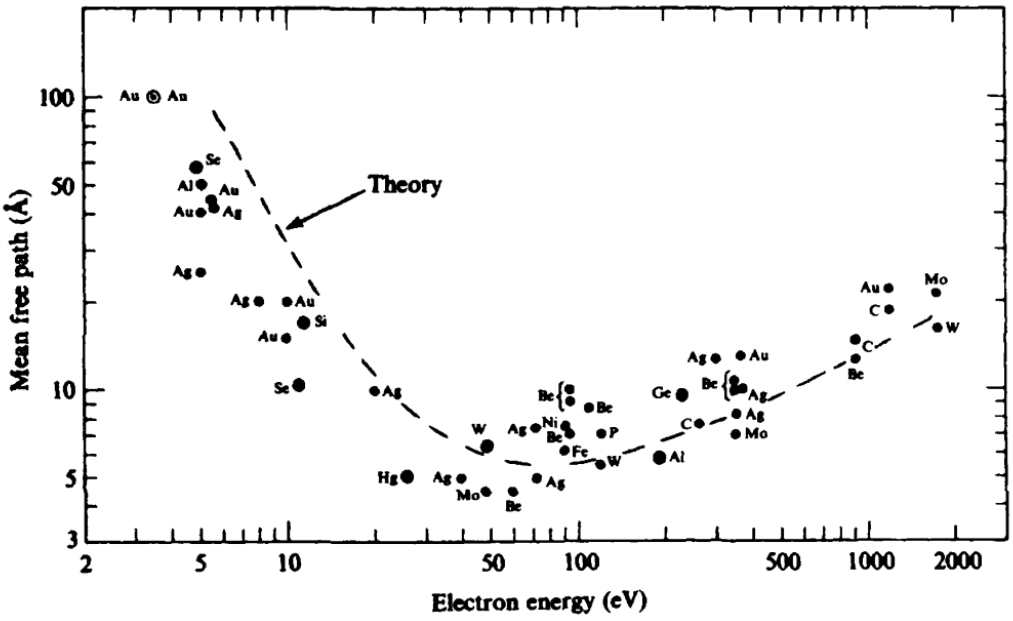

FIG. 2.2. Universal curve of electron mean free path: experiment (Rhodin & Gadzuk, 1979; Somorjai, 1981); theory (Penn, 1976) [2].

For the un-scattered emitted electrons, their kinetic energy is related to the material electronic states. The binding energy of the electrons can be calculated using the following equation:

$$BE = h\nu - KE - \phi_w \qquad \text{Eq. (2.1)}$$

, where BE represents the electron binding energy, hν represents the photon energy, KE represents the electron kinetic energy after emission and ϕ_w represents the work function

of the material. This equation describes the well-known photoelectric effect. The kinetic energy measured from experiment is usually defined with respect to the vacuum level of the spectrometer. Since sample and spectrometer are aligned at the Fermi Level, equation (2.1) can be rewritten as follows:

$$\mathrm{BE} = \mathrm{h}\nu - \mathrm{KE} - \phi_s + qV \qquad \text{Eq. (2.2)}$$

, where BE is the electron binding energy relative to the vacuum level, hν is the photon energy, KE is the measured kinetic energy, ϕ_s is work function of spectrometer, q is elementary charge and V is the bias applied between sample and electron analyzer. The bias is used to accelerate electrons, to overcome the spectrometer work function and thus to improve the collection of the low kinetic energy electrons.

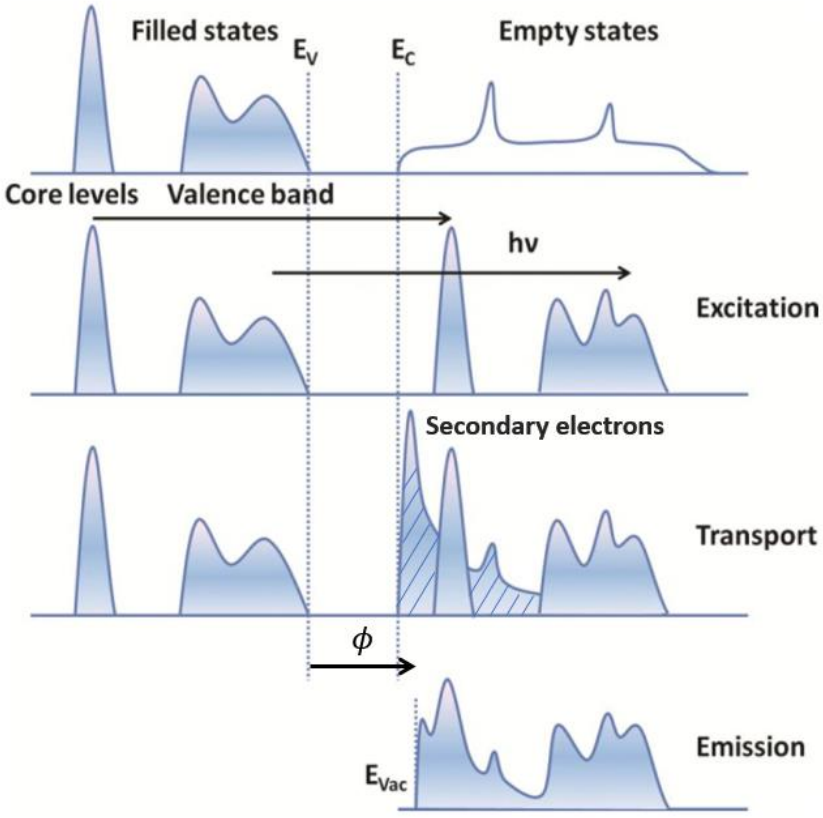

FIG. 2.3. PES described as a three-step model: (1) photoexcitation of electrons, which are excited from filled states to empty conduction band states; (2) electrons transport to the surface while producing secondary electrons due to in inelastic collisions; (3) electrons with energy greater than the work function escape from the surface into vacuum and contribute to the photoemission spectrum.

Depending on the light source, PES systems can be divided into three groups: ultra-violet photoemission spectroscopy (UPS); soft x-ray photoemission spectroscopy (SXPS) and x-ray photoemission spectroscopy (XPS). The photon energy ranges of these systems are 0-100 eV, 100-1000 eV and > 1000 eV for UPS, SXPS and XPS, respectively. In our research, UPS and XPS were employed to study the electronic states. UPS has a relatively

high surface sensitivity, high resolution and is extensively used for valence-band characterization. In addition, UPS is used to determine surface information such as work function and/or electron affinity. However, since the UV photon energy is relatively low, UPS only provides information on shallow core levels. XPS, on the other hand, can be used in studies of the valence band as well as the core-level regimes. The higher photon energy enables measurements of deeply bound electrons. In our research, we combine XPS and UPS measurements, exploiting the comparatively larger sampling depth and the core level information of XPS and the high resolution and surface sensitivity of UPS.

2.2.2 PES Systems in NSL

Two of the three PES systems in the NSL were involved in the studies related to this dissertation: the VG Scienta XPS/UPS system and the VSW UPS system.

The VG Scienta XPS/UPS integrated PES system is a newly constructed system with a base pressure of $\sim 1 \times 10^{-9}$ Torr. It consists of a Scienta MX 650 high intensity monochromatic Al K_α x-ray source (1486.7 eV) with a bandwidth of 0.2 eV, a Prevac UVS 40A2 high intensity UV source optimized for He I and He II radiation at 21.22 eV and 40.82 eV, respectively, and a Scienta R3000 hemisphere high-resolution electron energy analyser for both XPS and UPS measurements. A 750 nm thick aluminum foil separates the x-ray monochromator and main chamber. A picture of this system is shown in FIG. 2.4. The x-ray and UV light spots are aligned at the center of the sample in order to obtain information from same spot. An image of the x-ray and UV spots focused on a phosphors screen is shown in FIG. 2.5.

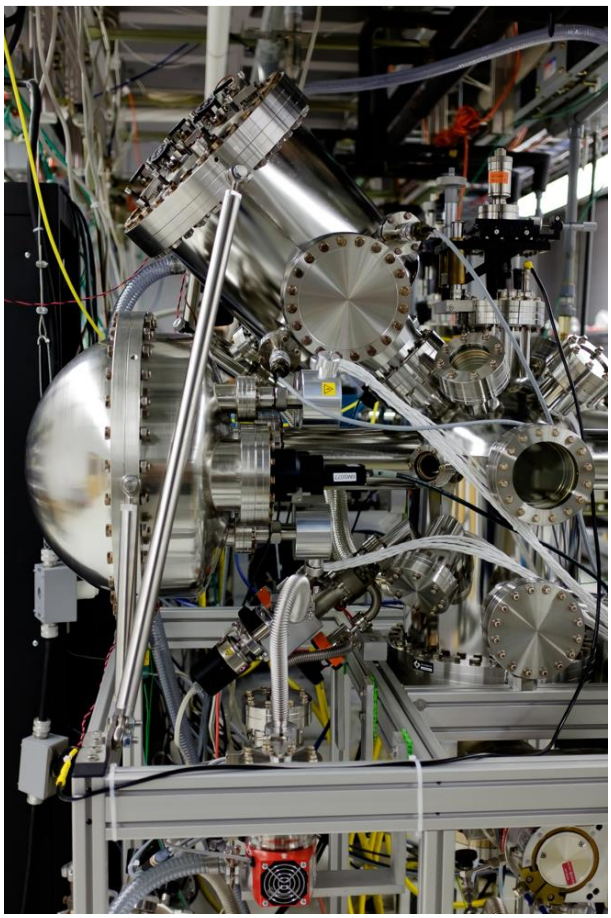

FIG. 2.4. A view of the NSL VG Scienta XPS/UPS integrated PES system.

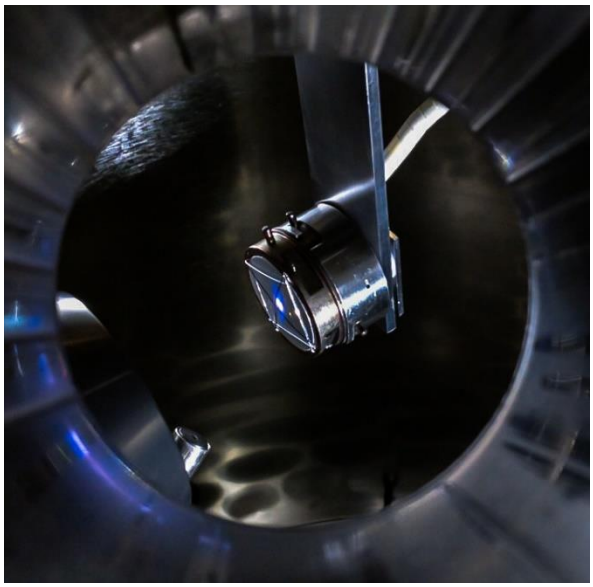

FIG. 2.5. A view of the x-ray (blue) and UV (white) spots focused on a phosphors screen.

The x-rays in this system are produced by fine focused electron beam bombardment on a water-cooled aluminum anode from a tungsten cathode. The size of the electron beam on the anode is ~1 × 3 mm, which equals to the size of the x-ray spot on the sample after focusing by the monochromator. The monochromator consists of seven 76 mm diameter, toroidal α-quartz crystals. One quartz crystal is located at the center and six quartz crystals are positioned in a circle around the center crystal. All seven crystals are placed on a Rowland circle of 650 mm diameter. These quartz crystals are heated to 55 °C to avoid photon energy shifts caused by temperature changes during the measurements. The monochromatizating principle of the light is based on Bragg's law, and the focus is governed by the Rowland circle condition. The crystals diffract the x-ray according to Bragg's law:

$$2d \sin\theta = n\lambda \qquad \text{Eq. (2.3)}$$

, where d is the distance between two crystal lattice planes, θ is the reflective angle and λ is the incident light wavelength. The angles of the crystals are fixed, hence only a narrow band of x-rays will be diffracted onto the sample, which serves the purpose of monochromatizating and achieves a narrow band of 0.2 eV.

A Prevac UVS 40A2 is employed as the UV source. The operation of the UV source is based on a cold cathode capillary discharge. Research grade helium is used for the discharge. To improve the vacuum in the main PES chamber, the UV source employs differential pumping. The source is optimized for He I and He II radiation by adjusting the discharge current and the discharge gas pressure.

A Scienta R3000 hemispherical analyzer is shared for the XPS and UPS measurements. It has a mean radius of 135 mm. Electrons emitted from the sample first

pass through an elaborate multi-element electrostatic lens to collect and transfer electrons from sample to a 0.2 × 20 mm curved slit. The lens focuses electrons in two modes (transmission mode and angular mode) and changes electron initial kinetic energy to a desired energy range by applying an accelerating field. The center of this desired energy band is defined as the mean analyzing energy, or pass energy. Then electron energy dispersion is performed by the positively charged inner sphere and negatively charged outer sphere. Finally, the electrons transit to the detection system, which includes a field termination mesh, two multi-channel plates (MCP), a phosphorous screen and a CCD camera. The employment of a 2D CCD camera presents energy information in one direction and spatial/angular information in the other direction, which provides the ability to present an image of the energy versus angle of samples electronic states. A schematic for the R3000 analyzer is shown in FIG. 2.6. This analyzer yields a ~3 meV resolution when conducting UPS measurements operating at a 2 eV pass energy and a ~0.1 eV resolution when conducting XPS measurements at a 100 eV pass energy.

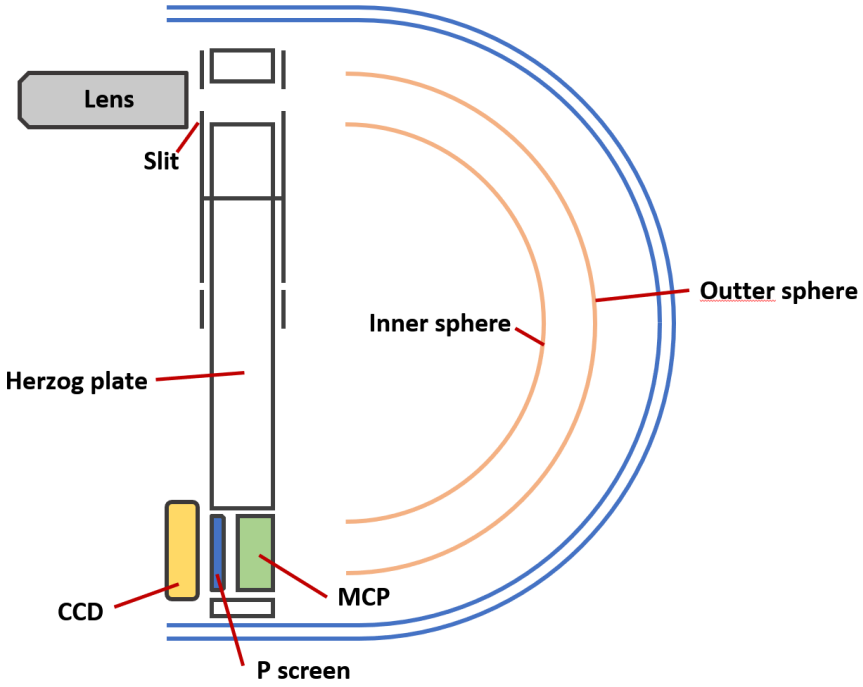

FIG. 2.6. Schematic for R3000 hemisphere electron energy analyzer.

The VSW UPS system operates with a similar principle as the one mentioned above with a few differences. There is a coil heater employed on the sample stage, so thermionic emission measurements could be conducted. The UV source is optimized for He I, He II and Ar I (11.83 eV) discharges. The VSW 50mm hemispherical analyzer is mounted on a two-angle goniometer, which allows 360° movement in the horizontal plane and 100° tilt in the vertical plane. For single crystal samples, this allows angle-resolved photoelectron spectroscopy analysis. In addition, the analyzer uses a Channeltron single channel electron multiplier, where only charge pulses are available for analysis. This system yields a resolution of approximately 1% of its applied pass energy.

2.2.3 Calibration of PES Systems

Since binding energy information is usually the primary characteristic for electronic states measurements, XPS and UPS spectra are commonly presented as plots of intensity vs binding energy. According to equation (2.2), the work function of the system needs to be known to convert measured kinetic energy into binding energy, which requires calibration of the photoemission spectroscopy systems. Freshly *in-situ* deposited metal or noble metal samples are normally used for calibration to avoid metal oxidation of the surface. In our case, a 0.05 mm thick gold foil with 99.95% purity was used for the calibration. Before calibration was conducted, the gold foil was cleaned *in-situ* with a hydrogen plasma in the electron cyclotron resonance (ECR) CVD system for surface contamination removal.

There are two common methods for PES system calibration. For XPS, the core level peak position of a known sample is aligned to the known value. For UPS, the position of a metal Fermi level is measured and then aligned to zero in the binding energy scale. As shown in FIG. 2.7, the 4f core level calibration spectra of a H-plasma cleaned Au sample, the Au $4f_{7/2}$ peak was aligned to 84.00 eV, and thus the work function of the system is determined.

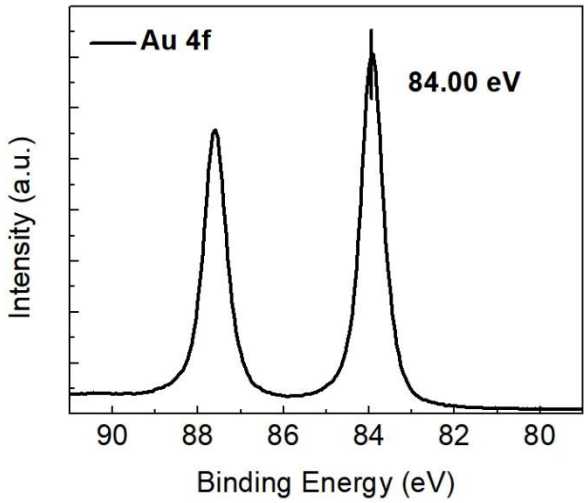

FIG. 2.7. The Au 4f core level spectra of a standard Au foil for XPS calibration.

An example of an UPS calibration spectra of a standard Au sample is shown in FIG. 2.8. A significant Fermi level cut-off edge is observed and aligned to zero in the binding energy scale. The work functions of the UPS systems was consequently determined.

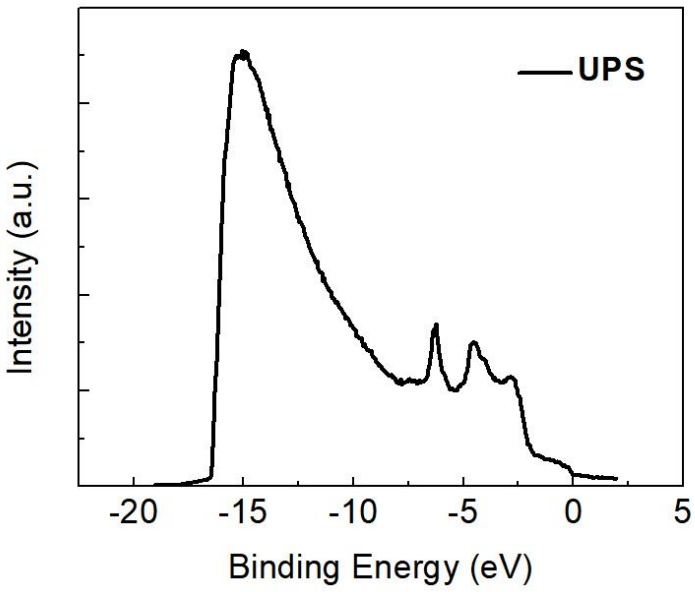

FIG. 2.8. UPS calibration scan of a H-plasma cleaned Au film.

2.3 Atomic Layer Deposition

2.3.1 Atomic Layer Deposition Principles

Atomic layer deposition (ALD) is a self-limiting sub monolayer deposition method. The process was first adopted by the semiconductor industry to improve the quality of high-k materials. With the development of this technology, ALD studies have expanded to metal nitrides, metal sulfides and elemental metal deposition. Compared to other film growth methods ALD has the advantage of precise deposition thickness control, uniform and conformal thin film deposition.

ALD is cycle-by-cycle process. In each cycle, there are four steps: first, a precursor is introduced into chamber and a self-limiting reaction will affect the surface; then, nitrogen is used to remove the excess precursor and byproducts from the chamber; afterwards, an oxidization step is conducted and oxygen replaces the ligands; last, another nitrogen purge is used to remove the excess oxygen and gaseous byproducts from the chamber and prepare the surface for the next cycle.

Depending on the oxygen reactant types, ALD can be divided into different categories. Thermal ALD often uses water or gaseous molecules as the reactant. The reactions between precursor attached to the surface and reactant are driven by thermal energy. Plasma-enhanced ALD (PEALD) employs plasma generated atomic species and radicals instead of water or gaseous molecules, which results in more reactive reactants. FIG. 2.9 shows principles of a plasma system. Oxygen gas transports through a high frequency electric field. This field provides accelerates electrons and creates a non-equilibrium condition between the electron temperature and gas temperature. This leads to conversion of the oxygen gas into electrons and oxygen species including O^{2+}, O^{2-}, O^{+}, O^{-},

O_2 and O. Because of the increased reactivity of these oxygen species, they actively react with precursor molecules on the sample surface. Higher film growth rate, improved film density, reduced impurity levels and enhanced electronic properties can be achieved with the introduction of an oxygen plasma process. The increased reactivity leads to lower deposition temperature and increases the choice of precursors and substrates. In addition, the plasma process introduces additional deposition controlling parameters, such as operating pressure, plasma power, plasma exposure time and even mixed plasmas. Controlling these parameters of the oxygen plasma may help optimize the ALD growth process. However, PEALD also has drawbacks, such as plasma-induced damage, reduced conformality and step coverage.

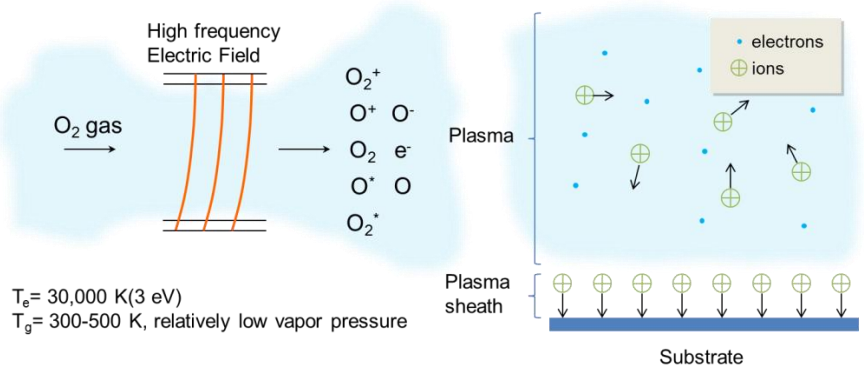

FIG. 2.9. Schematic of the inductively coupled oxygen plasma.

2.3.2 PEALD ZnO Deposition

In order to reduce the plasma-induced damage, a remote plasma is employed in our system. FIG. 2.10 shows a schematic of the remote PEALD system. The PEALD system uses a 13.56 MHz radio frequency (RF) inductively coupled plasma to create reactive species and radicals. The remote plasma is generated about 25 cm above the samples stage.

Five different kinds of precursors can be directed into the chamber using argon as a carrier gas and supplied through the top side into the chamber. A heater coil below the sample holder can heat samples to the growth temperature. The chamber temperature is maintained at about 100 ºC to avoid condensation on the chamber walls. The system has a base pressure of ~5 × 10^{-8} Torr.

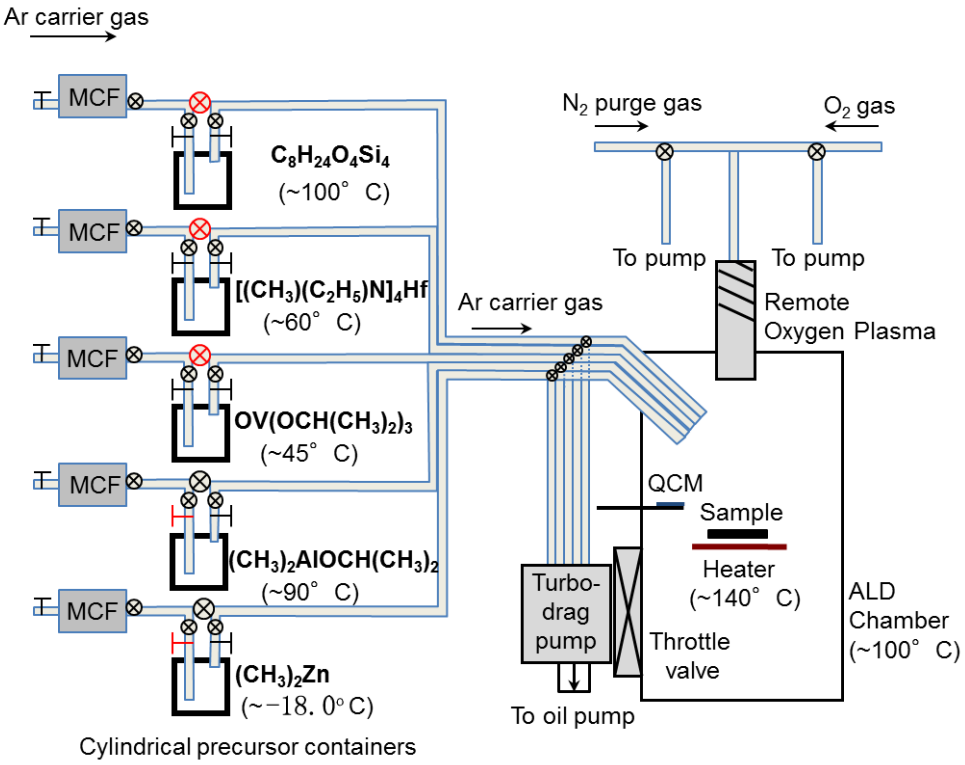

FIG. 2.10. Schematic of the NSL remote PEALD system.

In the dissertation related research, ZnO PEALD deposition was conducted using the system mentioned above. A plasma-enhanced ALD deposition cycle for ZnO with dimethylzinc (DMZ) precursor is shown in FIG. 2.11. ZnO thin films can be grown in a temperature range from 100 to 350°C using the thermal ALD method [4-6]. With PEALD, the deposition temperature can be decreased to 80 °C, which enables the use of substrates that require a low processing temperature, such as plastic. In our experiments, dimethylzinc

is used as the precursor. Because of the high vapor pressure of DMZ at room temperature, the precursor container is cooled to -18 °C in a chiller. During the deposition, 50 standard cubic centimeters per minute (sccm) of Ar gas was used as a carrier gas to transport the precursor into the reaction chamber. The substrate was heated to 100 °C, and the chamber pressure was controlled at 100 mTorr. During the plasma step, 35 sccm oxygen gas was input, and the generation power was set to 200 W. Pulse times for zinc precursor, nitrogen purge and oxygen plasma are 0.35 s, 40 s and 8 s, respectively. With this configuration, a deposition rate of 2.0 Å/cycle was measured by Rutherford backscattering spectrometry (RBS).

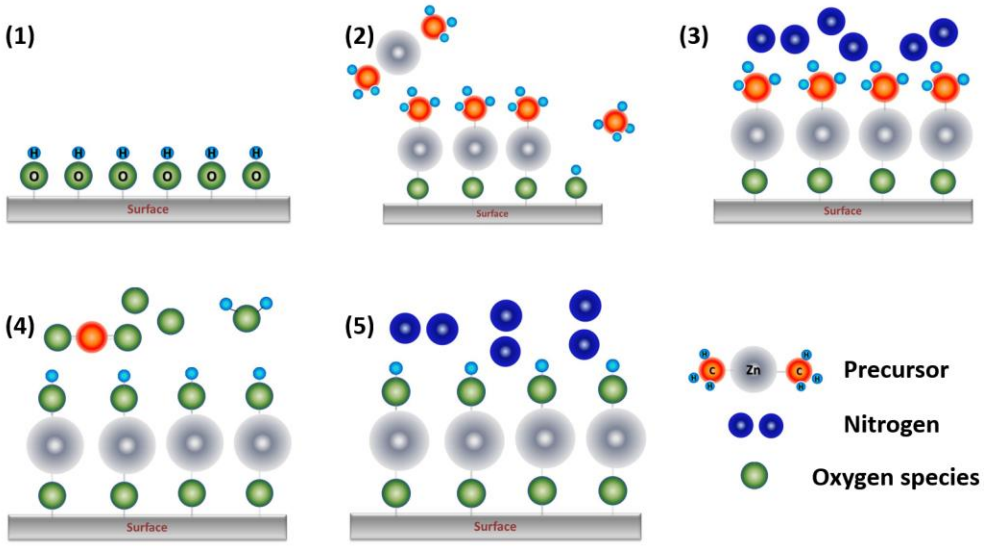

FIG. 2.11. An illustration of the ZnO PEALD deposition steps using DMZ precursor and oxygen plasma: (1) the initial surface, (2) precursor self-limiting reaction at the surface, (3) N_2 purge to remove excess precursor and byproducts, (4) O-plasma species react with adsorbed precursor molecules, (5) N_2 purge to remove excess reactant and byproducts and prepare the surface for the next cycle.

2.4 Chemical Vapor Deposition for Diamond Growth

Diamond becomes attractive as an ultra-wide bandgap semiconductor because its extreme properties such as highest thermal conductivity, high electrical breakdown field, and high hole mobility. Diamond was first synthesized using the high-pressure high-temperature method (HPHT) reported by General Electric [7]. The modern era of chemical vapor deposition of diamond growth started in the 1980s [8].

Various enhanced CVD systems have been demonstrated for diamond growth. However, they share important common features. First, atomic hydrogen is employed in the process. It was reported that atomic hydrogen etches graphite at a higher rate than diamond structure carbon, which provides a selective etching process during growth. In addition, assisted dissociation of carbon-containing source gases is typically required since the thermal CVD process can only provide very slow growth for diamond because of the high activation energy of methane decomposition. Consequently, energy enhanced CVD methods can provide more energy, which results in a higher growth rate. Finally, a moderate growth temperature is necessary. A substrate temperature between 500 ~ 1200 °C is usually used during the growth. A higher or lower temperature results in graphite or diamond-like-carbon (DLC) deposition [9]. A standard model for CVD diamond growth is described as follows: the diamond lattice and surface are stabilized by hydrogen atom termination; in the gas phase, reactive carbon-containing radicals are created with hydrocarbon species; on the surface, radical sites are created with the abstraction of hydrogen from the surface C-H bonds; finally, carbon incorporates into the lattice and converts into sp^3 bonded carbon.

In our research, a SEKI style plasma enhanced chemical vapor deposition (PECVD) system is employed for diamond growth. Microwave plasma provides energy to excite the gas phase molecules (H_2 and C_xH_y), which then generate atomic hydrogen and hydrocarbon species:

$$H_2 \rightarrow 2\ H,$$

$$CH_4 + H \rightarrow CH_3 + H_2,$$

A schematic of the PECVD system is shown in FIG. 2.12. An ASTeX microwave plasma source (5kW maximum output power) operates at 2.455 GHz frequency. The base pressure of the system is ~10^{-8} Torr through turbo molecular pumping. Source gases were H_2 as atomic hydrogen source, CH_4 as the carbon source and TMP (trimethylphosphine) diluted with H_2 as the phosphorus source. The sample is immersed in the plasma and heated only by the plasma, which reduces the impurities in the diamond film. A picture of a sample immersed in a plasma is shown in FIG. 2.13.

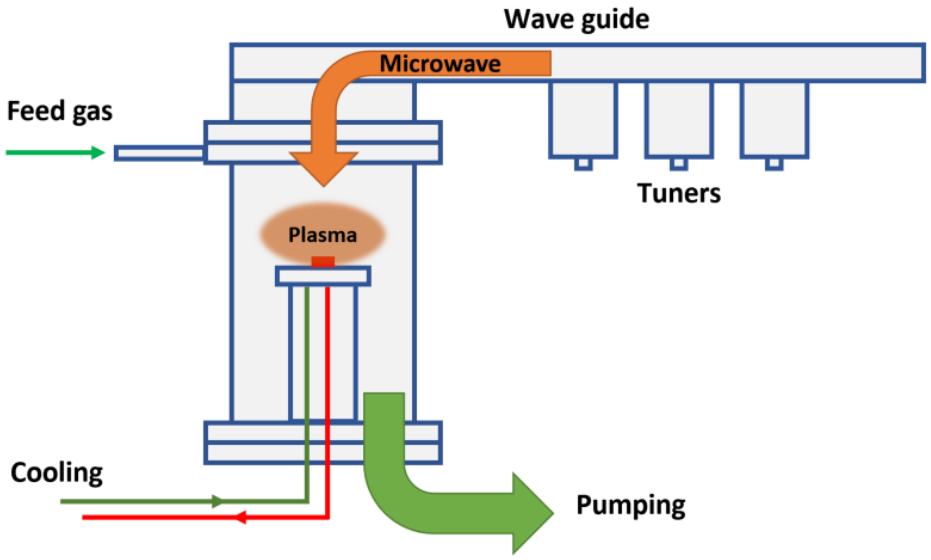

FIG. 2.12. A schematic for diamond PECVD systems.

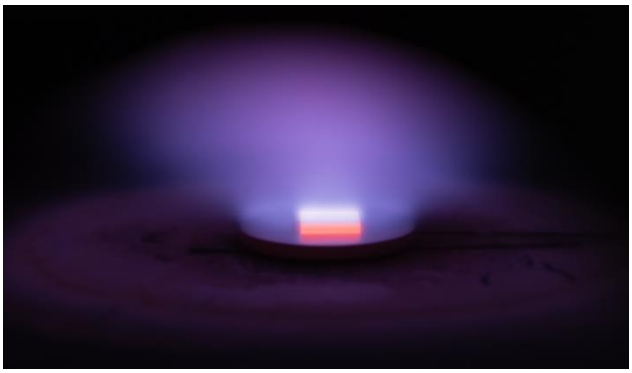

FIG. 2.13. A picture of a sample immersed in plasma.

2.5 Characterization with Photoemission Spectroscopy

2.5.1 Electron Affinity

The electron affinity (EA) is defined as the energy to add an electron onto a material, which equals the energy difference between vacuum level (E_{VL}) to conduction band minimum (CBM). UPS is often employed for electron affinity measurements. With UPS, the electron affinity value can be determined using:

$$\mathrm{EA} = \mathrm{h}\nu - \mathrm{W} - E_g \qquad \text{Eq. (2.4)}$$

, where hν is the photon energy, W is the width of the UPS spectra and E_g is the bandgap of the material.

2.5.2 Band Bending

A method to determine the band bending (BB) of a sample was proposed by Waldrop *et al.*, which depends on XPS core level measurements and inherent material properties [10]. The band bending can be calculated with the following equation:

$$BB = (E_{CL} - E_V)_{substrate} + E_g - E_{CL} - E_C \qquad \text{Eq. (2.5)}$$

, where $(E_{CL} - E_V)_{substrate}$ is the difference between the core level and the valence band maximum, a constant for a certain material; E_g is the band gap of the material; E_{CL} is the XPS measured core level position and E_C is the conduction band minimum of the material. Based on this method, the band bending of a material can be calculated with XPS measurements.

However, because of the XPS probe depth, this method is only correct when the depletion region is significantly larger than 3 ~ 10 nm. If the width of the depletion region is close to the probe depth of XPS, equation 2.5 must be modified to account for the quadratic nature of the bands in the depletion region.

UPS provides another way to determine the band bending:

$$BB = E_g - E_C - E_V \qquad \text{Eq. (2.6)}$$

, where E_g is the band gap of the material; E_C is the conduction band minimum of the substrate, and E_V is the UPS measured valence band maximum value.

2.5.3 Band Alignment

PES is a valuable tool to investigate the electronic states at semiconductor interfaces. For metal/semiconductor interfaces, the Schottky barrier height could be deduced from the PES measurements with the following equation [11]:

$$\Phi_B = E_g - E_{core}^f + \left(E_{core}^i - E_{VBM}^i\right) \qquad \text{Eq. (2.7)}$$

, where E_g is the room temperature band gap of the semiconductor, E_{core}^f is the final semiconductor core level position after metal deposition, E_{core}^i and E_{VBM}^i are the semiconductor core level and the VBM value for the surface before metal deposition,

respectively. PES is also widely employed in semiconductor/semiconductor interface studies. Waldrop and Grant, and Kraut et al. proposed a photoemission method to investigate semiconductor band offset in 1980s [12-15]:

$$VBO = (E_{CL} - E_{VBM})_1 - (E_{CL} - E_{VBM})_2 + \Delta E_{CL} \quad \text{Eq. (2.8)}$$

, where VBO is the valence band offset; $(E_{CL} - E_{VBM})_1$ is the difference between the core level and the valence band maximum for semiconductor 1; $(E_{CL} - E_{VBM})_2$ is the difference between the core level and the valence band maximum for semiconductor 2; and ΔE_{CL} is the core level difference at the interface.

2.5.4 Film Thickness

The XPS peak intensities can be used to determine the interface layer thickness. The photoelectron signal intensity is attenuated in the film at a distance z from the surface, and the total peak intensity is provided by [15,16]:

$$I = \int I_0 e^{-z/\lambda}\, dz \quad \text{Eq. (2.9)}$$

, where I_0 is the photoemission intensity from the atoms at the surface, and λ is the photoelectron inelastic mean free path. When XPS peak areas are obtained before and after film deposition, the area ratio can be used to calculate the film thickness based on this equation.

References

1. Franciosi, A. and C.G. Van de Walle, *Heterojunction band offset engineering*. Surface Science Reports. Vol. 25. 1996. 1-140.

2. Zangwill, A., *Physics at surfaces*. 1988: Cambridge University Press.

3. Hüfner, S., *Photoelectron Spectroscopy Principles and Applications. 3 ed*. 2003: Springer-Verlag Berlin Heidelberg.

4. Lim, S.J., S. Kwon, and H. Kim, *ZnO thin films prepared by atomic layer deposition and rf sputtering as an active layer for thin film transistor*. Thin Solid Films, 2008. 516(7): p. 1523-1528.

5. Wójcik, A., M. Godlewski, E. Guziewicz, R. Minikayev, and W. Paszkowicz, *Controlling of preferential growth mode of ZnO thin films grown by atomic layer deposition*. Journal of Crystal Growth, 2008. 310(2): p. 284-289.

6. Lujala, V., J. Skarp, M. Tammenmaa, and T. Suntola, *Atomic layer epitaxy growth of doped zinc oxide thin films from organometals*. Applied Surface Science, 1994. 82-83: p. 34-40.

7. Nassau, K. and J. Nassau, *The history and present status of synthetic diamond.* Journal of Crystal Growth, 1979. 46(2): p. 157-172.

8. Kato, H., T. Makino, S. Yamasaki, and H. Okushi, *N-type diamond growth by phosphorus doping on (001)-oriented surface.* Journal of Physics D: Applied Physics, 2007. 40(20): p. 6189-6200.

9. Gracio, J.J., Q.H. Fan, and J.C. Madaleno, *Diamond growth by chemical vapour deposition.* Journal of Physics D: Applied Physics, 2010. 43(37): p. 374017.

10. Waldrop, J.R. and R.W. Grant, *Measurement of AlN/GaN (0001) heterojunction band offsets by x-ray photoemission spectroscopy.* Applied Physics Letters, 1996. 68(20): p. 2879-2881.

11. Coppa, B.J., C.C. Fulton, S.M. Kiesel, R.F. Davis, C. Pandarinath, J.E. Burnette, R.J. Nemanich, and D.J. Smith, Structural, *Microstructural, and electrical properties of gold films and Schottky contacts on remote plasma-cleaned, n-type ZnO{0001} surfaces.* Journal of Applied Physics, 2005. 97(10): p. 103517.

12. Kraut, E.A., R.W. Grant, J.R. Waldrop, and S.P. Kowalczyk, *Precise Determination of the Valence-Band Edge in X-Ray Photoemission Spectra: Application to Measurement of Semiconductor Interface Potentials.* Physical Review Letters, 1980. 44(24): p. 1620-1623.

13. Waldrop, J.R., E.A. Kraut, S.P. Kowalczyk, and R.W. Grant, *Valence-band discontinuities for abrupt (110), (100), and (111) oriented Ge-GaAs heterojunctions.* Surface Science, 1983. 132(1-3): p. 513-518.

14. Waldrop, J.R. and R.W. Grant, *Semiconductor Heterojunction Interfaces: Nontransitivity of Energy-band Discontiuities.* 1988. 1: p. 287-290.

15. Wang, X., C. Campbell, Y.-H. Zhang, and R.J. Nemanich, *Band alignment at the CdTe/InSb (001) heterointerface.* Journal of Vacuum Science and Technology, A, 2018. 36: p. 031101.

16. Kerkhof, F.P.J.M. and J.A. Moulijn, *Quantitative-Analysis of XPS Intensities for Supported Catalysts*. Journal of Physical Chemistry, 1979. 83(12): p. 1612-1619.

CHAPTER 3

BAND ALIGNMENT AT THE CDTE/INSB (001) HETEROINTERFACE

3.1 Abstract

CdTe/InSb heterojunctions have attracted considerable attention because of its almost perfect lattice match and the presence of non-octal interface bonding. This heterojunction is a model heterovalent system to describe band offsets. In this research, molecular beam epitaxy was used to deposit a ~5 nm epitaxial CdTe (001) layer on an InSb (001) surface. Monochromatic x-ray photoemission spectroscopy and ultra-violet photoemission spectroscopy were used to characterize the electronic states of clean InSb and CdTe surfaces and CdTe/InSb (001) heterostructures. A room temperature remote hydrogen-plasma process was used to clean the surfaces prior to characterization. The results indicate a valence band offset of 0.89 eV and a type-I (straddling gap) alignment for the CdTe/InSb (001) heterostructure interface. In addition, In-Te bonding was observed at the interface. Downward band bending of the InSb is attributed to excess electrons introduced by non-octal In-Te interface bonding.

(In collaboration with Calli Campbell, Yong-Hang Zhang and Robert J. Nemanich.)

3.2 Introduction

Heterojunctions of II-VI and III-V semiconductors have been studied for several decades. The CdTe/InSb heterojunction is a model heterovalent system because of its almost perfect lattice match and the potential for non-octal interface bonding. Electron-counting methods have been used for qualitative analysis of the interface bonding. For zincblende structure II-VI and III-V semiconductors, the group II, III, V, and VI elements, respectively, contribute 2/4, 3/4, 5/4, and 6/4 of an electron to the tetrahedral bonds. In the bulk, bonding stability relies on the tetrahedral bonding arrangement, and a full complement of two electrons in each bond. While at heterointerfaces, bonds between III and VI atoms give 9/4 e^- and bonds between II and V atoms give 7/4 e^-, which yields an excess or deficit of 1/4 e^-, respectively. These non-octal bonding configurations across heterovalent interfaces act as donors or acceptors in adjacent layers, and affect the carrier distribution and band bending at interfaces. For the zincblende structure, an ideally terminated (001) surface would display a single kind of atom. Thus, if an abrupt interface forms between II-VI and III-V semiconductors, the bonding at the interface is anticipated to be between II-V atoms or III-VI atoms. In this case, non-octal bonding, which provides an unbalance of electrons, can occur at each type of interface. This makes understanding the interface electronic state properties considerably more complicated than isovalent interfaces [1,2]. As an example, the CdTe/GaAs heterojunction has shown an excess interface electron density of ~1×10^{14} cm^{-2} [3]. Based on the electron counting method, atomic interface models were proposed to explain the heterointerface charge [2,4,5].

CdTe and InSb are both zincblende structure and have a small room temperature lattice mismatch ($|\Delta a|/a \leq 5\times10^{-4}$) [6]. Early reports of II-VI/III-V heterojunctions focused on the interface band alignment. For the CdTe/InSb heterojunction, an experimental valence band offset (VBO) of 0.87 ± 0.1 eV was reported. However, the interface bonding and the charge distribution were left unclear [7]. Recently reported cross-sectional transmission electron microscopy (XTEM) results on CdTe/InSb (001) heterojunctions similar to those studied here show exceptional structural quality and an interface without visible extended defects. In addition, the absence of extensive interfacial compounds other than an atomically thin layer was suggested [8]. These heterojunctions also show optimum optical and electronic properties because of their low interface defect density [9,10]. In this report, we present photoemission spectroscopy results on CdTe/InSb (100) heterojunctions. The PES results indicate that an interface layer of ~1.5 nm mainly with In-Te bonding occurs between InSb and CdTe. The heterojunction shows type-I band alignment and band bending consistent with the presence of an electron accumulation layer on the InSb side of the interface.

3.3 Experiment

The samples were grown on commercially obtained n-type single crystal (001) InSb substrates (doped with Te at ~5×10^{17} atoms/cm^3). The InSb and CdTe epitaxial growth processes were performed in a dual-chamber molecular beam epitaxy system, which consists of separate II-VI and III-V growth chambers connected by an ultra-high vacuum (UHV) preparation chamber. The InSb surfaces were prepared by thermal oxide desorption

at 476-480 °C under an Sb flux (all substrate temperatures measured by an optical pyrometer). Following the oxide removal step, a 600 nm InSb buffer layer was grown at 390 °C. The sample was then transferred under UHV to the II-VI growth chamber. The sample temperature was ramped gradually (10 °C/min) to 250 °C, wherein the surface was flooded with Cd to prevent undesired reactions between group III (In) and group VI (Te) elements as the substrate temperature was ramped further to 280 °C. At 280 °C, a Te flux was then supplied at a Cd to Te flux ratio of 3:1 and a Te-limited growth rate of 1.6 Å/s was measured by reflection high energy electron diffraction. The CdTe film thickness was determined to be 4.5 nm from x-ray photoemission spectroscopy (XPS) analysis.

For band alignment measurements, the samples were transferred to the NanoScience Lab UHV system, which consists of six sample preparation and deposition chambers, five surface characterization chambers and an ~22 m long UHV transfer line that connects all the processing and characterization chambers. Prior to loading, the samples were cleaned with a jet of ultra-high purity nitrogen gas. To minimize the effects from contaminants, an in-situ room temperature remote hydrogen-plasma process was used prior to the photoemission experiments. The research-grade hydrogen flow rate was set to 90 standard cubic centimeters per minute (sccm). The plasma was excited using RF power (13.56 MHz, 100 W) applied to a helical copper coil wrapped around a ~32 mm diameter quartz tube. The base of the quartz tube was ~200 mm away from the sample. The remote plasma generated predominantly atomic H with low densities of ions and excited neutrals. The surface contamination was monitored using XPS scans of the carbon and oxygen 1s spectra.

The band offsets and band bending were deduced from *in-situ* XPS and ultra-violet photoemission spectroscopy (UPS) measurements. The XPS system consists of a high intensity monochromatized Al Kα x-ray source (1486.7 eV) with a bandwidth of 0.2 eV and a Scienta R3000 high-resolution electron energy analyzer with a resolution of 0.1 eV. The core level peaks were analyzed using CasaXPS, and peak positions could be determined with a relative uncertainty of 0.05 eV. Two UPS systems both optimized for He I radiation at 21.2 eV were used for the measurements. One system, which used the R3000 analyzer operating with 2 eV pass energy yielding an analyzer resolution of 3 meV, was employed for InSb valence band scans. A VSW HAC 50 mm mean radius hemispherical analyzer operating in FAT mode with 15 eV pass energy, which has a resolution of 0.15 eV, was utilized for CdTe on InSb valence band scans. During the UPS scans, a bias of -4.0 V or -8.0 V was applied to the substrate to overcome the work function of the analyzer. The photoemission systems were calibrated using a plasma cleaned gold foil.

3.4 Results

The hydrogen plasma cleaning process provides a lower cleaning temperature compared with thermal desorption cleaning, which limits antimony desorption, retains the sample stoichiometry, and mitigates surface roughening [11,12]. The XPS results of the carbon and oxygen 1s core levels of InSb and CdTe/InSb before and after H-plasma cleaning are shown in FIG. 3.1. In FIG. 3.1 (b-i), the Sb $3d_{5/2}$ peak from antimony oxide and the O 1s peak merged together. After the H-plasma clean, the carbon, antimony oxide and

oxygen peaks were below the XPS detection limit, indicating the species were effectively removed. The stoichiometry analysis based on the XPS peak intensities indicates that the composition of the CdTe film was retained.

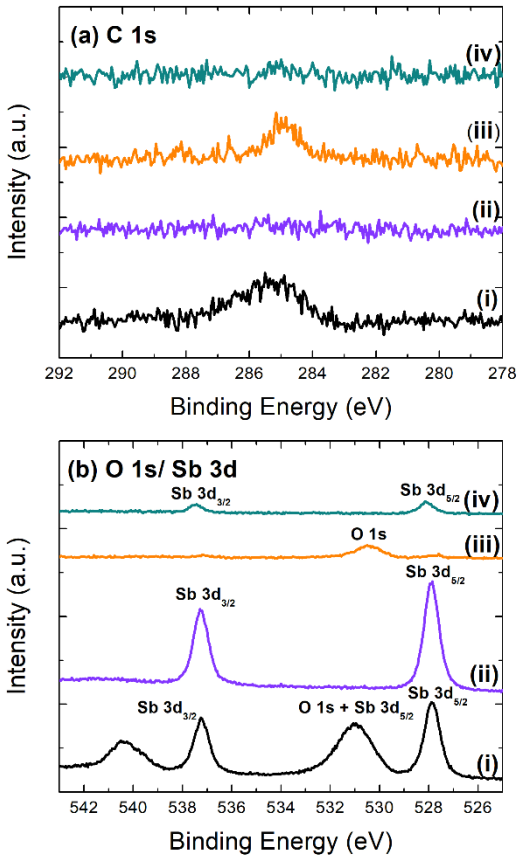

FIG. 3.1. X-ray photoemission spectroscopy scans of (a) the C 1s peak and (b) the O 1s and Sb 3d peak. The scans were as follows: (i) InSb before the H-plasma clean, (ii) InSb after 5 min. H-plasma clean, (iii) CdTe on InSb before H-plasma clean, and (iv) CdTe on InSb after 30 s H-plasma clean.

The XPS scans of the H-plasma cleaned InSb and CdTe/InSb heterojunction are presented in FIG. 3.2. The In and Sb 3d intensities are noticeably lower after the CdTe thin film deposition indicating the coverage of the CdTe film. After CdTe deposition, the Sb

peak does not show a noticeable shoulder. Thus, the Sb 3d core-level shift was used to determine the InSb band bending. After CdTe deposition, the Sb $3d_{3/2}$ and $3d_{5/2}$ core-level energies increased 0.2 eV, which indicates a 0.2 eV downward band bending.

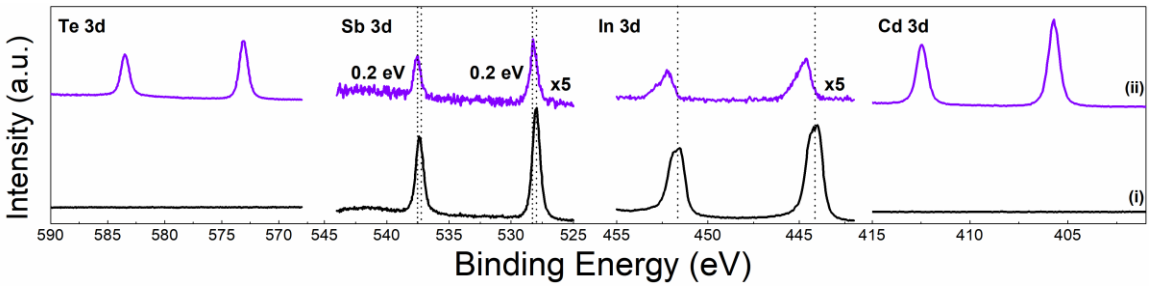

FIG. 3.2. From left to right: XPS spectra for Te 3d, Sb 3d, In 3d and Cd 3d peaks (i) H-plasma cleaned InSb and (ii) H-plasma cleaned CdTe/InSb.

XPS was also employed to investigate the low binding energy regime which ranged from the Sb 4d peaks to the valence band maximum (VBM). The results are shown in FIG. 3.3. A 0.2 eV shift to higher binding energy was observed for the Sb 4d peaks, which is consistent with the 3d peak shifts. To determine the VBO of the CdTe/InSb heterojunction, the Sb 4d peaks were aligned to the same position as shown in FIG. 3.3. Scan (i) determines the InSb VBM relative to the Sb 4d level, and scan (ii) determines the VBM of the CdTe layer relative to the Sb 4d level in the heterostructure. The difference of the Sb 4d to VBM of the two scans was 0.9 eV, which is used to determine the VBO. Consequently, a VBO of 0.9 eV was determined between InSb and CdTe in the CdTe/InSb heterojunction.

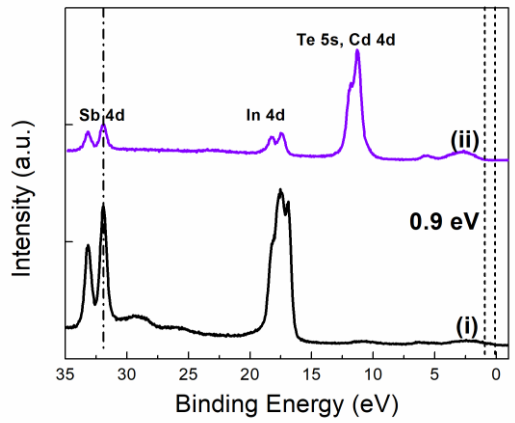

FIG. 3.3. XPS scans for close to VBM regime (i) InSb substrate (ii) after CdTe deposition.

Ultra-violet (21.2 eV) photoemission spectra after H-plasma cleaning are presented in FIG. 3.4. For the InSb surface, the VBM was measured at 0.11 eV below the Fermi level, and for the CdTe surface (on the InSb substrate), the VBM was located 1.2 eV below the Fermi level.

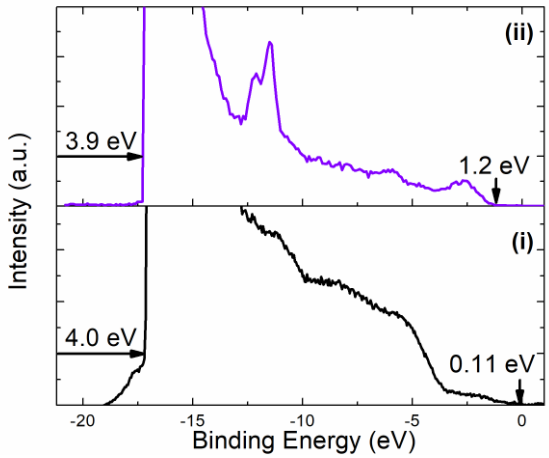

FIG. 3.4. Ultra-violet photoemission spectra of (i) InSb surface and (ii) CdTe on InSb.

The PES results are summarized in TABLE 3.1. Electron affinity (χ) values were calculated using the following equation:

$$\chi = \phi + E_{VBM} - E_g \qquad \text{Eq. (3.1)}$$

, where ϕ is the work function of the surface, E_{VBM} is the relative difference between the valence band maximum and Fermi level, and E_g is the band gap of the material. For the calculation, 1.51 eV was used for the CdTe band gap and 0.17 eV was used for the InSb band gap [13,14].

TABLE 3.1. XPS fitting results for Cd 3d, Te 3d, In 3d and Sb 3d core levels and VBO; UPS results for valence band maximum value (E_{VBM}) and work function (ϕ); and deduced results for electron affinity (χ). All the values are presented in electron-volt.

Surface	Cd 3d	Te 3d	In 3d	Sb 3d	E_{VBM}	ϕ	χ	VBO
InSb	--	--	444.1/451.6	527.9/537.2	0.11	4.0	3.9	--
CdTe on InSb	405.6/412.4	473.0/483.4	444.5/452.0	528.1/537.4	1.2	3.9	3.6	0.9

3.5 Discussion

3.5.1 Interface Layer

As shown in FIG. 3.5, shoulder peaks that appeared in the In 3d and Te 3d spectra suggest the existence of indium-tellurium bonding. Meanwhile, no obvious shoulder peak is observed in the Cd 3d and Sb 3d spectra, which indicates the absence of Cd-Sb bonding. The shoulder peaks are located at 452.7 eV, 445.1 eV for the In 3d peaks and 582.8 eV, 572.4 eV for the Te 3d peaks. As reported in previous studies, multiple phases of indium telluride could be components at the interface. InTe and In_2Te_3 are two possible phases [7]. It has been reported that surface Sb atoms are volatile at ~300 °C [15,16]. Thus, during the CdTe deposition, the excess Sb atoms could evaporate from the surface.

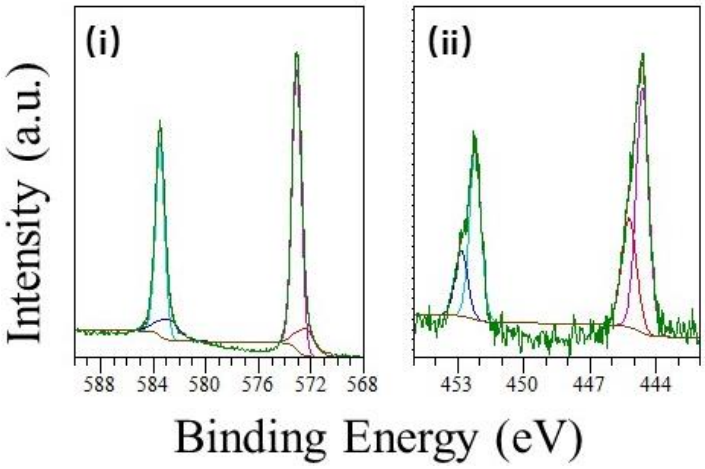

FIG. 3.5. Peak fitting analysis for XPS spectra of hydrogen-plasma cleaned CdTe on InSb: (i) Te 3d and (ii) In 3d peaks.

XPS peak intensities were used for the interface layer thickness calculation. Abrupt CdTe/In-Te layer/InSb interfaces are assumed during the calculation. Wolfram Mathematica was employed to solve the integral equations. The photoelectron signal intensity is attenuated in the film at a distance z from the surface, and the total peak intensity is provided by [17]:

$$I = \int I_0 e^{-z/\lambda} dz \qquad \text{Eq. (3.2)}$$

, where I_0 is the photoemission intensity from the atoms at the surface, and λ is the photoelectron inelastic mean free path. The inelastic mean free path of In 3d, Sb 3d and Te 3d core level photoemission electrons were 2.6, 2.1 and 2.0 nm respectively obtained using the TPP-2M equation [18,19].

Before the interface layer thickness calculation, the total thickness of the CdTe layer and interface layer was calculated using the Sb 3d peak intensities. The post- and pre-CdTe deposition peak intensity ratio is measured to be 0.12. Thus, we have:

$$0.12 = \frac{\int_{t_{Total}}^{\infty} I_0 e^{-z/\lambda} dz}{\int_0^{\infty} I_0 e^{-z/\lambda} dz} \quad \text{Eq. (3.3)}$$

, where t_{Total} is the total thickness of the CdTe layer and interface layer, and it was determined to be 4.5 nm based on the above equation. Then, the interface layer thickness was calculated based on the In 3d and Te 3d peaks, respectively. The shoulder peak of the In 3d was considered to be from In-Te bonding in the interface layer, and the main peak was from In-Sb bonding. The ratio of the shoulder peak to full peak area can be calculated as

$$ratio_{In3d} = \frac{\int_{t_{Total}-t_{Interface}}^{t_{Total}} I_0 e^{-z/\lambda} dz}{\int_{t_{Total}-t_{Interface}}^{\infty} I_0 e^{-z/\lambda} dz} \quad \text{Eq. (3.4).}$$

From XPS analysis, the area ratio between shoulder peak and full peak is measured to be 0.37, which indicated an interface layer thickness of 1.2 nm.

When calculating the interface layer thickness from the Te 3d peak, the Te 3d main peak was considered to contribute to the Cd-Te bonding, and the shoulder peak was attributed to In-Te bonding. Similarly, the area ratio of the shoulder peak and full peak can be calculated using:

$$ratio_{Te3d} = \frac{\int_{t_{Total}-t_{Interface}}^{t_{Total}} I_0 e^{-z/\lambda} dz}{\int_0^{t_{Total}} I_0 e^{-z/\lambda} dz} \quad \text{Eq. (3.5)}$$

, with the measured area ratio of 0.18, an interface layer thickness of 1.8 nm was determined. Since the CdTe film is close to the surface, the In-Te layer contribute relatively

weaker signal to the Te 3d peak compared with the CdTe layer, which may lead to uncertainty when calculating peak area ratio. Besides, in the calculation based on the In 3d peak area, the total thickness of the CdTe layer and interface layer is not involved. However, it is employed in the interface layer thickness calculation based on the Te 3d peak intensity, which may be responsible for the discrepancy of interface layer thicknesses deduced from the In 3d and Te 3d peaks. Taking the average, we consider the interface layer thickness to be ~1.5 nm.

3.5.2 Band Alignment Schematic

The valence band offset could also be calculated using the method proposed by Waldrop and Grant, and Kraut et al. [20-22]:

$$VBO = (E_{CL}^{InSb} - E_{VBM}^{InSb}) - (E_{CL}^{CdTe} - E_{VBM}^{CdTe}) - \Delta E_{CL} \qquad \text{Eq. (3.6)}$$

, where E_{CL}^{InSb} , and E_{CL}^{CdTe} represent the respective binding energies of the Sb and Cd 3d core levels, E_{VBM}^{InSb} , E_{VBM}^{CdTe} represent the InSb and CdTe valence band maxima measured by UPS, and ΔE_{CL} is the Sb and Cd 3d core level difference at the interface. The calculation indicates a VBO value of 0.89 eV, which is consistent with the value of 0.9 eV from the XPS valence band edge measurement described in Sec. 3.4.

The schematic band alignment for the CdTe and InSb heterojunction is presented in FIG. 3.6. It is notable that a type I semiconductor heterojunction is observed with this structure. In addition, a 0.2 eV downward band bending appears at the InSb side of the interface.

3.5.3 Interface Charge Model

According to the XPS analysis, the bonds at the heterointerface are between In and Te atoms. The downward band bending at the boundary of InSb and CdTe could be caused by charge transfer from donor-type bonds at the heterointerface. Since each In-Te bond contributes 9/4 electrons (instead of two electrons for octal bonding), each In-Te bond provides 1/4 excess electron and acts as a donor. The free movement of these excess electrons allows accumulation at the InSb side of the heterointerface since the InSb conduction band minimum (CBM) is lower than the CdTe CBM. The excess electrons could separate into a depletion region of several nanometers in the InSb.

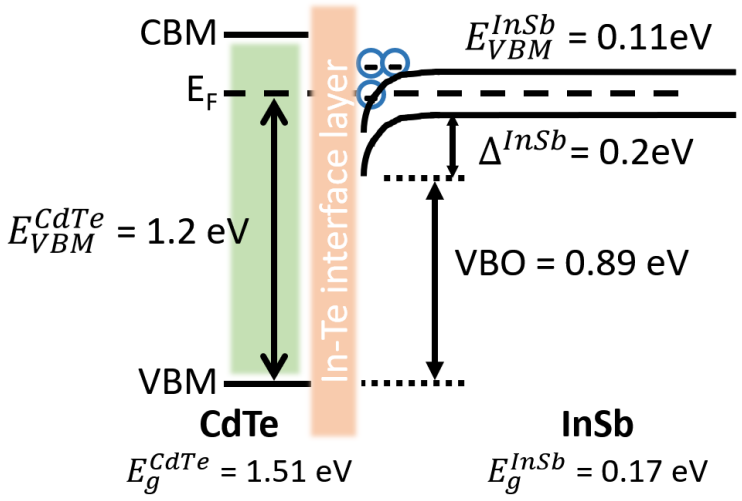

FIG. 3.6. Schematic of band alignment of CdTe/InSb heterojunction.

However, it needs to be noted that the CBM of InSb extends below the Fermi level at the interface, and electrons could accumulate in the conduction band. The high density of accumulated electrons could cause sharp downward band bending in a small region close to the interface layer. This sharp band bending would be difficult to detect using XPS; thus, the actual band bending at the interface could be larger than 0.2 eV.

3.6 Summary and Conclusions

In this research, MBE was used for the growth of a CdTe/InSb (100) heterostructure. A room temperature H-plasma was found to be an efficient way to clean air-exposed InSb and CdTe surfaces. The XPS results indicated the existence of In-Te bonding at the interface, and the peak analysis indicated the formation of a ~1.5 nm interface layer. The band alignment of the CdTe/InSb heterostructure was deduced from XPS and UPS measurements. A type-I heterojunction was observed with a valence band offset of 0.89 eV. The CdTe on InSb can confine both electrons and holes in the InSb. The donor-type bonds between In and Te would provide 1/4 e^- on average leading to an electron accumulation layer at the InSb side of the interface.

Acknowledgments

This research was supported through the National Science Foundation under Grant No. DMR-1206935, Department of Energy Bay Area Photovoltaic Consortium (BAPVC) under Award No. DE-EE0004946 and Air Force Office of Scientific Research (AFOSR) Grant No. FA9550-15-1-0196.

References

1. Franciosi, A. and C.G. Van de Walle, *Heterojunction band offset engineering.* Surface Science Reports, 1996. 25(1-4): p. 1-140.

2. Frey, A., U. Bass, S. Mahapatra, C. Schumacher, J. Geurts, and K. Brunner, *Band offsets and band bending at heterovalent semiconductor interfaces.* Physical Review B, 2010. 82(19).

3. Xi, S., W. Jie, G. Zha, Y. Yuan, T. Wang, W. Zhang, J. Zhu, L. Xu, Y. Xu, J. Su, H. Zhang, Y. Gu, J. Li, J. Ren, and Q. Zhao, *Effects of Ga-Te interface layer on the potential barrier height of CdTe/GaAs heterointerface.* Phys. Chem. Chem. Phys., 2016. 18(4): p. 2639-2645.

4. Dandrea, R.G., S. Froyen, and A. Zunger, *Stability and band offsets of heterovalent superlattices: Si/GaP, Ge/GaAs, and Si/GaAs.* Physical Review B, 1990. 42(5): p. 3213-3216.

5. Farrell, H.H., M.C. Tamargo, J.L. de Miguel, F.S. Turco, D.M. Hwang, and R.E. Nahory, *"Designer" interfaces in II-VI/III-V polar heteroepitaxy*. Journal of Applied Physics, 1991. 69(10): p. 7021-7028.

6. Farrow, R.F.C., G.R. Jones, G.M. Williams, and I.M. Young, *Molecular beam epitaxial growth of high structural perfection, heteroepitaxial CdTe films on InSb (001).* Applied Physics Letters, 1981. 39(12): p. 954-956.

7. Mackey, K.J., P.M.G. Allen, W.G. Herrenden-Harker, R.H. Williams, C.R. Whitehouse, and G.M. Williams, *Chemical and electronic structure of InSb-CdTe interfaces.* Applied Physics Letters, 1986. 49(6): p. 354-356.

8. Lu, J., M.J. DiNezza, X.-H. Zhao, S. Liu, Y.-H. Zhang, A. Kovacs, R.E. Dunin-Borkowski, and D.J. Smith, *Towards defect-free epitaxial CdTe and MgCdTe layers grown on InSb (001) substrates.* Journal of Crystal Growth, 2016. 439: p. 99-103.

9. Zhao, X.-H., M.J. DiNezza, S. Liu, C.M. Campbell, Y. Zhao, and Y.-H. Zhang, *Determination of CdTe bulk carrier lifetime and interface recombination velocity of CdTe/MgCdTe double heterostructures grown by molecular beam epitaxy*. Applied Physics Letters, 2014. 105(25): p. 252101.

10. Zhao, Y., M. Boccard, S. Liu, J. Becker, X.-H. Zhao, C.M. Campbell, E. Suarez, M.B. Lassise, Z. Holman, and Y.-H. Zhang, *Monocrystalline CdTe solar cells with open-circuit voltage over 1 V and efficiency of 17%.* Nature Energy, 2016. 1(6): p. 16067.

11. Bell, G.R., N.S. Kaijaks, R.J. Dixon, and C.F. McConville, *Atomic hydrogen cleaning of polar III-V semiconductor surfaces.* Surface Science, 1998. 401(2): p. 125-137.

12. Jaime-Vasquez, M., M. Martinka, A.J. Stoltz, R.N. Jacobs, J.D. Benson, L.A. Almeida, and J.K. Markunas, *Plasma-Cleaned InSb (112)B for Large-Area Epitaxy of HgCdTe Sensors.* Journal of Electronic Materials, 2008. 37(9): p. 1247-1254.

13. Fonthal, G., L. Tirado-Mejía, J.I. Marín-Hurtado, H. Ariza-Calderón, and J.G. Mendoza-Alvarez, *Temperature dependence of the band gap energy of crystalline CdTe.* Journal of Physics and Chemistry of Solids, 2000. 61(4): p. 579-583.

14. Littler, C.L. and D.G. Seiler, *Temperature dependence of the energy gap of InSb using nonlinear optical techniques.* Applied Physics Letters, 1985. 46(10): p. 986-988.

15. Stariy, S.V., A.V. Sukach, V.V. Tetyorkin, V.O. Yukhymchuk, and T.R. Stara, *Effect of thermal annealing on electrical and photoelectrical properties of n-InSb.* Semiconductor Physics Quantum Electronics and Optoelectronics, 2017. 20(1): p. 105-109.

16. Liu, J. and T. Zhang, *Rapid thermal annealing characteristics of Be implanted into InSb.* Applied Surface Science, 1998. 126(3-4): p. 231-234.

17. Kerkhof, F.P.J.M. and J.A. Moulijn, *Quantitative-Analysis of XPS Intensities for Supported Catalysts.* Journal of Physical Chemistry, 1979. 83(12): p. 1612-1619.

18. Tanuma, S., C.J. Powell, and D.R. Penn, *Calculations of electron inelastic mean free paths. VIII. Data for 15 elemental solids over the 50-2000 eV range.* Surface and Interface Analysis, 2005. 37(1): p. 1-14.

19. Powell, C.J. and A. Jablonski, *NIST Electron Inelastic-Mean-Free-Path Database - Version 1.2.* 2010: National Institute of Standards and Technology.

20. Kraut, E.A., R.W. Grant, J.R. Waldrop, and S.P. Kowalczyk, *Precise Determination of the Valence-Band Edge in X-Ray Photoemission Spectra: Application to Measurement of Semiconductor Interface Potentials.* Physical Review Letters, 1980. 44(24): p. 1620-1623.

21. Waldrop, J.R. and R.W. Grant, *Semiconductor Heterojunction Interfaces: Nontransitivity of Energy-band Discontinuities.* Physical Review Letters, 1979. 43(22): p. 1686-1689.

22. Waldrop, J.R., E.A. Kraut, S.P. Kowalczyk, and R.W. Grant, *Valence-band discontinuities for abrupt (110), (100), and (111) oriented Ge-GaAs heterojunctions.* Surface Science, 1983. 132(1-3): p. 513-518.

CHAPTER 4

BAND ALIGNMENT OF COPPER ON ZN- AND O- FACE ZNO (0001) AND POLYCRYSTALLINE ZNO

4.1 Abstract

ZnO has a spontaneous polarization of 0.047 C/m^2. The work function of Cu is close to the electron affinity of ZnO, thus the polarization effects could be important in determining the electronic properties of Cu/ZnO interfaces. Importantly, Cu/ZnO heterointerfaces have been widely used in methanol synthesis. The band alignment of Cu/ZnO interfaces will enable understanding the properties of metal/ZnO interfaces and the catalytic effects that enable methanol synthesis. In this research, n-type ZnO (0001) and (000$\bar{1}$) surfaces were pretreated using an O/He plasma, and clean polycrystalline ZnO surfaces were obtained by plasma-enhance atomic layer deposition (PEALD). Using these starting surfaces, monochromatic x-ray photoemission spectroscopy (XPS) and ultra-violet photoemission spectroscopy (UPS) were used to characterize the electronic states of the ZnO surfaces and Cu/ZnO interfaces. The results indicate a 0.3 eV Schottky barrier at the Cu/ZnO (0001) interface and a zero barrier height at the Cu/ZnO (000$\bar{1}$) and Cu/PEALD ZnO interfaces. The low barrier heights are attributed to the formation of a copper-oxide interface layer. In addition, the polarization effects may contribute to the difference of the barrier heights.

(In collaboration with Manpuneet Kaur Benipal and Robert J. Nemanich.)

4.2 Introduction

Research on ZnO as a semiconductor can be traced back to the 1960s [1, 2]. Zinc oxide as a wide band gap semiconductor has a direct band gap of 3.4 eV. It has been considered for optoelectronic and microelectronic applications [3, 4]. The ZnO bulk Fermi level is typically located ~0.3 eV below the conduction band minimum (CBM) [5, 6], and the n-type conductivity has been attributed to defects including oxygen vacancies and zinc interstitials. However, the unintentional incorporation of hydrogen impurities has also been considered in recent studies [7]. Zinc oxide commonly exhibits the hexagonal wurtzite crystal structure [8], which results in the polar characteristics of the ZnO (0001) (Zn-face) and $(000\bar{1})$ (O-face) surfaces. Over the last few decades, considerable progress has been achieved in zinc oxide crystal and thin film growth, doping and device design. Since electrical contacts play an important role in the performance of devices such as blue/UV light emitting diodes, gas sensors and transparent conducting oxides, there is an emerging demand for better understanding of the electrical properties of the metal/zinc oxide interface. A comprehensive review article summarized the status of metal/zinc oxide interfaces [4], where it is noted that ZnO exhibits a behavior between covalent and ionic semiconductors, which makes the metal/ZnO interface band alignment difficult to predict. The formation of an interface layer between a metal and ZnO could also introduce defects into the ZnO, which may behave as donors or acceptors. In addition, it has been observed that O-face ZnO typically shows a lower barrier height than Zn-face ZnO, which suggests that the polarization effects at the metal contact behavior [4].

Cu/ZnO interfaces are especially interesting since copper has a work function of 4.6 eV, which is slightly higher than the electron affinity of zinc oxide (χ=4.0~4.3 eV) [9].

The basic theory of Schottky contact formation indicates that $\phi_B = \phi_M - \chi_S$ for n-type semiconductors [10]. Thus, this small difference between the metal work function and semiconductor electron affinity should yield a low Schottky barrier or ohmic contact, where the ZnO polarization could play an important role in determining the contact characteristics [11]. Moreover, the Cu/ZnO interface is industrially used as a catalyst in methanol synthesis [12]. The band alignment at the Cu/ZnO interface could help understand and improve the catalytic process. In this study, x-ray photoemission spectroscopy and ultra-violet photoemission spectroscopy have been employed to determine the band alignment of Cu/ZnO interfaces. In order to determine the effects of polarization, copper contacts were formed on high quality single crystal ZnO (0001), and $(000\bar{1})$ surfaces and PEALD polycrystalline ZnO films. The crystalline interfaces have high and opposite polarization, in contrast with the PEALD ZnO, which shows a polycrystalline structure, and a reduced average surface polarization [13].

4.3 Experiment

The interface characterization was conducted in an ultra high vacuum (UHV) system that integrates several chambers for sample preparation, growth, and surface characterization. The chambers are connected by a linear transfer line, which has a base pressure of ~5 × 10^{-10} Torr. This UHV environment enables *in-situ* photoemission spectroscopy (PES) measurements after each process step without atmospheric contamination.

Double-side polished wurtzite single crystal (0001) ZnO substrates were commercially obtained from MTI corporation. The substrate size was 10 mm × 10 mm ×

0.5 mm with zinc (0001) and oxygen ($000\bar{1}$) faces. According to the supplier, the substrates were grown using the hydrothermal method. Before the samples were loaded into the UHV system, the single crystal samples were rinsed with acetone and methanol, then ultra-high purity (UHP) nitrogen was used to dry the substrates. After loading into the UHV system, the surfaces were cleaned *in-situ* with a remote plasma using 20% O_2 and 80% He. Research-grade helium and oxygen were input through a quartz tube mounted at the top of the chamber. The plasma was excited with 20 to 40 W of 13.56 MHz RF applied to a copper coil wrapped around the quartz tube. The O_2 and He gas flow rates were 15 sccm and 60 sccm, respectively. The pressure in the chamber was kept at 50 mTorr. The zinc oxide samples were heated to 300 ~ 350 °C during the remote plasma cleaning and were cooled to room temperature in the unignited plasma ambient. After the cleaning procedure, copper deposition was performed in an electron-beam physical vapor deposition (EBPVD) system with a source purity of 99.9999%. The filament current was set to ~140 mA, and the pressure rose to ~1×10^{-7} Torr during deposition. The copper film thickness was monitored by a quartz crystal microbalance (QCM) and targeted at ~3 nm. XPS and UPS measurements were conducted after each process.

Virginia Semiconductor Inc. P-doped Si (100) (P doping concentration ~5×10^{18} atoms/cm^3) was chosen as the substrate for PEALD ZnO deposition because of its relatively low resistance, which reduces sample charging effects during the PES measurements. First, the Si substrates were cleaned in ultra-sonic acetone and methanol baths. Then, samples were dried using UHP nitrogen and loaded into the UHV system. An oxygen plasma process in the PEALD chamber was conducted to remove residual surface contamination. After oxygen treatment of the Si substrates, an amorphous layer of silicon

dioxide was formed. The SiO_2 layer could further retard the formation of large ZnO crystalline domains consequently leading to a reduced average polarization at the ZnO film surface. Dimethylzinc (DMZ) was used as the zinc precursor in the PEALD deposition. During the deposition, the substrates were heated to 100 °C, and the chamber pressure was controlled at 100 mTorr. The plasma generation power was set to 200 W. Pulse times for the zinc precursor and oxygen plasma were 0.35 s and 8 s, respectively. A deposition rate of 2.0 Å/cycle was measured by Rutherford backscattering spectrometry (RBS). 100 cycles were applied to obtain a ~20 nm ZnO thin film on the silicon substrate [14]. After the PEALD deposition, a copper film was deposited in the above-mentioned EBPVD system. After each procedure, PES measurements were employed to characterize the interface electronic states.

The XPS measurements used a high intensity monochromatized Al K_α source (1486.7 eV), and the UPS measurements used a He I discharge lamp (21.2 eV). The spectra were acquired with a Scienta R3000 high-resolution electron energy analyzer for both sources. During the XPS measurement, a resolution of 0.1 eV was achieved. The peak positions were determined with a relative uncertainty of 0.05 eV by peak fitting using CasaXPS. During the UPS measurements, the analyzer was operated at a 2 eV pass energy yielding an analyzer resolution of 3 meV. A bias of - 4.0 V was applied to the substrate to overcome the work function of the analyzer. The PES systems were calibrated with a plasma cleaned gold foil.

4.4 Results

For as-received (0001) and $(000\bar{1})$ zinc oxide surfaces, notable downward band bending was observed at the surfaces. This has been attributed to an electron accumulation layer caused by a hydroxide layer on the zinc oxide surface [15]. It has been proposed that hydrogen atoms donate about 0.5 e^- to surface oxygen atoms [15]. This results in the formation of a shallow electron donor state ($H + O^{2-} \rightarrow OH^- + e^-$) and increases the carrier concentration and electron accumulation layer charge density. Thus, an efficient *in-situ* cleaning process for zinc oxide is critical. The XPS results of the carbon and oxygen 1s core levels before and after O/He plasma cleaning are shown in FIG. 4.1. Carbon contamination was essentially removed after the plasma cleaning, with the C 1s peak intensities reduced to below the XPS detection limit. The O 1s intensity increased after the O/He plasma cleaning, which could be attributed to removal of the surface contamination. In addition, the intensity of the higher binding energy shoulder peak decreased indicating removal of the hydroxide species on the zinc oxide surfaces. Thus, reproducibly clean surfaces were achieved using the O/He plasma cleaning process.

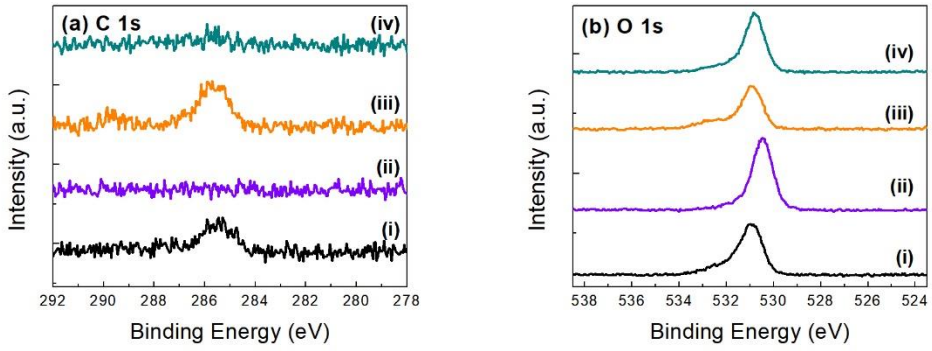

FIG. 4.1. XPS scans of (a) the C 1s peak and (b) the O 1s peak. The scans were: ZnO $(000\bar{1})$ (i) before O/He plasma clean, (ii) after O/He plasma clean and ZnO (0001) (iii) before O/He plasma clean, and (iv) after O/He plasma clean.

The XPS scans of the Zn and Cu 2p core levels after each step are shown in FIG. 4.2. The increase of the Zn 2p intensities after O/He plasma corresponds to the removal of surface contamination on the zinc oxide surface. After copper deposition, sharp Cu 2p peaks appeared, and the Zn 2p intensities decreased consistent with copper deposited on the surface.

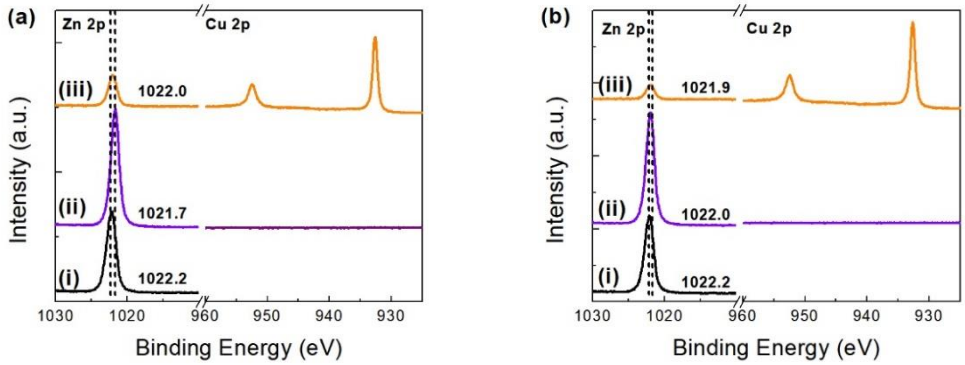

FIG. 4.2. The XPS Zn 2p and Cu 2p scans for (a) ZnO $(000\bar{1})$ and (b) ZnO (0001) surfaces (i) before O/He plasma clean, (ii) after O/He plasma clean and (iii) after ~3 nm Cu deposition.

The ultra-violet photoemission spectra are presented in FIG. 4.3. For bulk zinc oxide, since the Fermi level is typically located ~0.3 eV below the CBM, considering the ZnO band gap of 3.4 eV, the Fermi level is ~3.1 eV above valence band maximum (VBM) [5, 6]. According to FIG. 4.3, for the O-face after O/He plasma, the surface VBM was measured at 3.1 eV below the Fermi level, indicating flat bands at the surface. After copper deposition, the XPS Zn 2p peak shifted to higher binding energy indicating that downward band bending reoccurred at the interface. For the Zn-face, the UPS results indicated that the O/He plasma process reduced the initial downward band bending from 0.8 eV to 0.1 eV.

After copper deposition, the XPS Zn 2p peak shifted to lower binding energy, suggesting flat bands were obtained on the ZnO side of the interface.

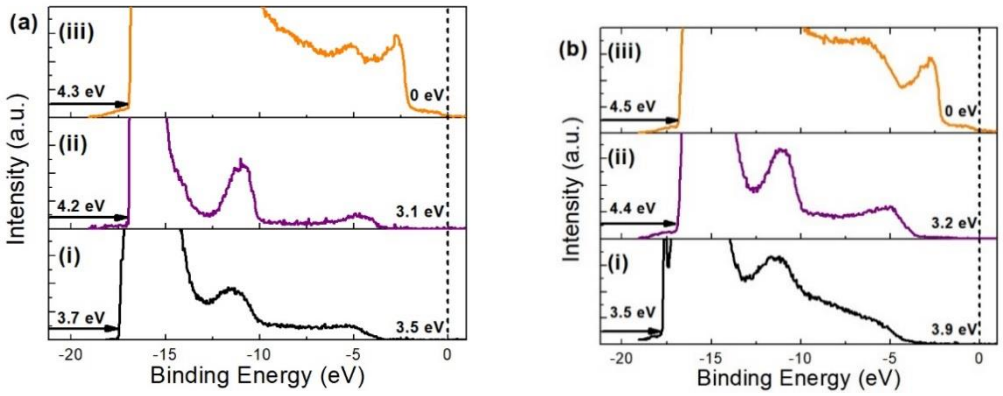

FIG. 4.3. Ultra-violet photoemission spectroscopy scans for (a) ZnO $(000\bar{1})$ and (b) ZnO (0001) surfaces (i) before O/He plasma clean, (ii) after O/He plasma clean and (iii) after ~3 nm copper deposition.

Photoemission spectra for the PEALD ZnO sample are presented in FIG. 4.4. After Cu deposition, the Zn 2p intensity decreased and the Cu 2p intensity increased, consistent with copper deposition on the ZnO film. For the as-deposited PEALD ZnO film, a VBM value of 3.1 eV was obtained by UPS, which indicates flat bands at the surface. After Cu deposition, the Zn 2p peak shifted to higher binding energy, indicating 0.3 eV downward band bending.

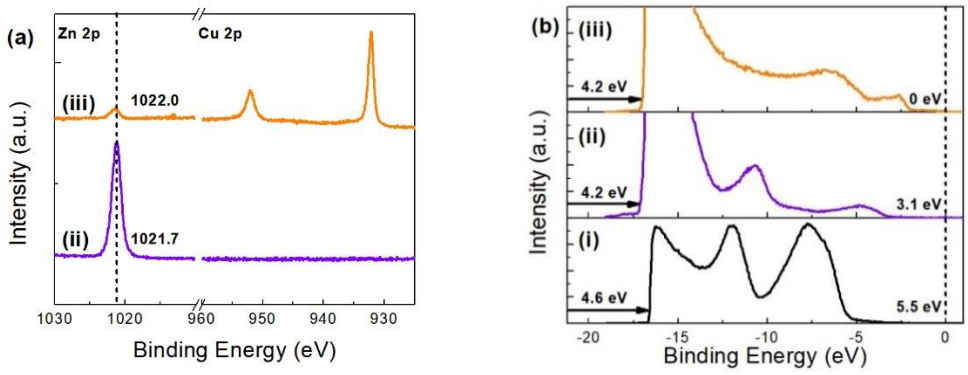

FIG. 4.4. (a) XPS and (b) UPS scans for: (i) clean silicon surface (ii) after 20 nm PEALD ZnO deposition and (iii) after ~3 nm copper deposition.

The PES results are summarized in TABLE 4.1, where the electron affinity values were calculated using the following equation:

$$\chi = \phi + E_{VBM} - E_g \qquad \text{Eq. (4.1)}$$

, where ϕ is the work function of the surface, E_{VBM} is the relative difference between valence band maximum and Fermi level and E_g is the band gap of the material. In this calculation, 3.4 eV is used for zinc oxide band gap.

The following equation was applied for Schottky barrier height calculations [5]:

$$\Phi_B = E_g - E_{core}^f + \left(E_{core}^i - E_{VBM}^i\right) \qquad \text{Eq. (4.2)}$$

, where E_g is the room temperature band gap of ZnO, E_{core}^f is the final Zn 2p core level position after copper deposition, E_{core}^i and E_{VBM}^i are the respective Zn 2p core level and the VBM values before metal deposition. Schottky barrier heights of 0, 0.3 eV and 0 are obtained for Cu/ZnO $(000\bar{1})$, Cu/ZnO (0001) and Cu/PEALD ZnO, respectively.

TABLE 4.1. Summary of XPS core level peak positions and E_{VBM} and ϕ from UPS. All values are in eV. Core level and VBM values are relative to the Fermi level.

Sample	Surface	Zn $2p_{3/2}$	O 1s	Cu 2p	E_{VBM}	ϕ	χ	ϕ_B
ZnO $(000\bar{1})$	Before plasma clean	1022.2	530.9	--	3.5	3.7	3.8	--
	After plasma clean	1021.7	530.5	--	3.1	4.2	3.9	--
	After Cu deposition	1022.0	530.8	932.6/952.4	0	4.3	--	0
ZnO (0001)	Before plasma clean	1022.2	530.9	--	3.9	3.5	4.0	--
	After plasma clean	1022.0	530.8	--	3.2	4.4	4.2	--
	After Cu deposition	1021.9	530.8	932.6/952.4	0	4.5	--	0.3
PEALD ZnO	Clean Si	--	532.9	--	5.5	4.6	1.2	--
	After 20 nm ZnO	1021.7	530.5	--	3.1	4.2	3.9	--
	After Cu deposition	1022.0	531.1	932.7/952.5	0	4.2	--	0

The band alignment of the different Cu/ZnO interfaces are shown in FIG. 4.5. As shown in the schematics, Cu/ZnO $(000\bar{1})$ and Cu/PEALD ZnO show a zero barrier height while Cu/ZnO (0001) shows a Schottky barrier height of ~0.3 eV.

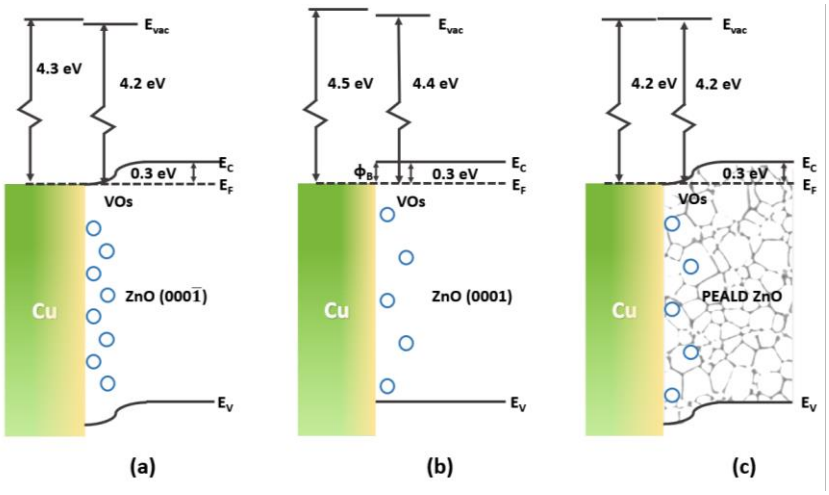

FIG. 4.5. Schematics of band alignments of Cu/ZnO interfaces for (a) ZnO $(000\bar{1})$, (b) ZnO (0001), and (c) PEALD ZnO.

4.5 Discussion

The metal/ZnO heterointerface is complicated because of the ZnO polar nature and extrinsic defects introduced during metal deposition. It is reported that metals such as Al, Ta, Ti and Ir react with oxygen in ZnO to form oxide interface layers, which may introduce defect states that lead to ohmic behavior [4, 16]. The introduced defects have been suggested to be oxygen vacancies [17, 18], which show donor-like behavior in ZnO [4, 19]. Moreover, it was found that the Zn-face ZnO yields a barrier height that is 0.1 to 0.2 eV higher than O-face ZnO [20, 21].

In our study, shoulder peaks were observed for the XPS Cu 2p peaks in all three samples, which is attributed to a copper oxide layer. The formation of copper-oxygen interface bonding indicates that oxygen atoms from ZnO migrate and bond to Cu in the deposited layer, which we propose results in oxygen vacancies in the near surface layer of ZnO. Because the near surface ZnO layer has native and the copper induced oxygen vacancies, a higher oxygen vacancy density is expected compared to the deeper ZnO. The donor-like behavior of oxygen vacancies introduces free electrons, which would diffuse into the ZnO because of the electron density gradient. A depletion region is formed between positively charged vacancies and free electron in the ZnO, and a downward band bending would be expected at the surface. Consequently, this results in lower barrier heights than anticipated.

Photoemission spectra peak fitting was conducted using CasaXPS to calculate the copper oxide layer thickness. The XPS photoelectron signal intensity is attenuated with an increase of the emission depth, and the total peak intensity can be calculated by [22]:

$$\mathrm{I} = \int I_0 e^{-z/\lambda} dz \qquad \text{Eq. (4.3)}$$

, where I_0 is the photoemission intensity from the atoms at the surface, z is the distance from the surface and λ is the photoelectron inelastic mean free path. Thus, the area ratio between the Cu 2p shoulder peak and total peak can be calculated as:

$$\text{ratio}_{Cu\ 2p} = \frac{\int_{t_{total}-t_{interface}}^{t_{total}} I_0 e^{-z/\lambda} dz}{\int_0^{t_{total}} I_0 e^{-z/\lambda} dz} \qquad \text{Eq. (4.4)}$$

, where t_{total} is 3 nm, the deposited copper film thickness measured by QCM, $t_{interface}$ is the thickness of the copper oxide interface layer, λ is the Cu 2p photoelectron inelastic mean free path (1.07 nm) [23, 24]. Based on the peak fitting results, the area ratios are 0.30, 0.25 and 0.30 for Cu/ZnO $(000\bar{1})$, Cu/ZnO (0001) and Cu/PEALD ZnO, respectively. These results indicate the copper oxide interface layer thicknesses as ~1.9 nm, ~1.7 nm and ~1.9 nm, respectively.

The different behavior of the two faces of wurtzite ZnO (0001) could contribute to the different results. It has been reported that the O-face typically shows more oxygen vacancies than the Zn-face even after plasma cleaning [21]. Thus, even before copper deposition, the O-face shows more oxygen vacancies originally. According to the calculation above, the copper-oxygen interface layers at three different Cu/ZnO interfaces show very similar thicknesses, and the density of deposition introduced oxygen vacancies is expected to be similar. Combining the original and deposition introduced oxygen vacancies, we suggest that the amount of oxygen vacancies at the Cu/Zn $(000\bar{1})$ interface is larger than the other configuration. Because the oxygen vacancies act as donors, which results in a lower barrier height, a zero barrier height was obtained at Cu/ZnO $(000\bar{1})$ interface. In contrast, there are fewer oxygen vacancies at the Cu/ZnO (0001) interface, and a 0.3 eV barrier height is observed.

As for the Cu/PEALD ZnO interface, a zero barrier height was also observed based on the photoemission spectroscopy measurements. When the ZnO film was deposited, the process started with a zinc precursor pulse and ended with an oxygen plasma step. Although the PEALD ZnO films show complicated polycrystalline structure, which reduces the average polarization, the films are more likely to be covered by oxygen atoms after the deposition. After copper films were deposited, these surface oxygen atoms are presumed to bond with the copper. The reduced polarization effects should result in a barrier height in between the barrier heights of Cu/Zn-face ZnO and Cu/O-face ZnO. However, the existence of grain boundaries and other defects introduced by the polycrystalline structure may contribute to the observed ohmic contact behavior.

4.6 Conclusion

In this study, copper thin films were deposited on ZnO (0001), (000$\bar{1}$) and PEALD zinc oxide surfaces. The single crystal ZnO surfaces were treated by O/He plasma. XPS was employed to characterize the pre-deposition surfaces. The band alignment of the different Cu/ZnO interfaces were deduced from PES measurements. A Schottky barrier height of 0.3 eV was observed at the Cu/ZnO (0001) interface. Zero barrier heights were observed at Cu/ZnO (000$\bar{1}$) and Cu/PEALD ZnO interfaces. The XPS results indicate that copper oxide appears at all interfaces, which implies the formation of oxygen vacancies in the ZnO due to Cu deposition. The lower than expected barrier heights are attributed to oxygen vacancies introduced by Cu-O bonding. In addition, it is proposed that the larger amount of oxygen vacancies at the ZnO (000$\bar{1}$) surface contribute to the 0.3 eV lower barrier height compared to ZnO (0001).

Acknowledgements

This research was supported by the National Science Foundation through Grant #DMR-1206935.

References

1. Reynolds, D.C. and T.C. Collins, *Excited Terminal States of a Bound Exciton-Donor Complex in ZnO.* Physical Review, 1969. **185**(3): p. 1099-1103.

2. Thomas, D.G., *The exciton spectrum of zinc oxide.* Journal of Physics and Chemistry of Solids, 1960. **15**(1-2): p. 86-96.

3. Look, D.C., *Recent advances in ZnO materials and devices.* Materials Science and Engineering: B, 2001. **80**(1-3): p. 383-387.

4. Brillson, L.J. and Y. Lu, *ZnO Schottky barriers and Ohmic contacts.* Journal of Applied Physics, 2011. **109**(12): p. 121301.

5. Jacobi, K., G. Zwicker, and A. Gutmann, *Work function, electron affinity and band bending of zinc oxide surfaces.* Surface Science, 1984. **141**(1): p. 109-125.

6. Kohl, D., M. Henzler, and G. Heiland, *Low temperature sublimation processes from clean cleaved polar surfaces of zinc oxide crystals during first heating.* Surface Science, 1974. **41**(2): p. 403-411.

7. Janotti, A. and C.G. Van de Walle, *Fundamentals of zinc oxide as a semiconductor.* Reports on Progress in Physics, 2009. **72**(12): p. 126501.

8. Göpel, W., L.J. Brillson, and C.F. Brucker, *Surface point defects and Schottky barrier formation on ZnO(10$\bar{1}$0).* Journal of Vacuum Science and Technology, 1980. **17**(5): p. 894-898.

9. Coppa, B.J., C.C. Fulton, S.M. Kiesel, R.F. Davis, C. Pandarinath, J.E. Burnette, R.J. Nemanich, and D.J. Smith, *Structural, microstructural, and electrical properties of gold films and Schottky contacts on remote plasma-cleaned, n-type ZnO{0001} surfaces.* Journal of Applied Physics, 2005. **97**(10): p. 103517.

10. Sze, S.M. and K.K. Ng, *Physics of Semiconductor Devices*. 2006, New York: Wiley.

11. Zúñiga-Pérez, J., V. Consonni, L. Lymperakis, X. Kong, A. Trampert, S. Fernández-Garrido, O. Brandt, H. Renevier, S. Keller, K. Hestroffer, M.R. Wagner, J.S. Reparaz, F. Akyol, S. Rajan, S. Rennesson, T. Palacios, and G. Feuillet, *Polarity in GaN and ZnO: Theory, measurement, growth, and devices.* Applied Physics Reviews, 2016. **3**(4): p. 041303.

12. Kattel, S., P.J. Ramírez, J.G. Chen, J.A. Rodriguez, and P. Liu, *Active sites for CO_2 hydrogenation to methanol on Cu/ZnO catalysts.* Science, 2017. **355**(6331): p. 1296-1299.

13. Benipal, M.K., *Photoinduced Charge Transfer at Metal Oxide/Oxide Interfaces Prepared with Plasma Enhanced Atomic Layer Deposition*. 2016, Arizona State University. p. 242.

14. Cheng, Q., M.K. Benipal, Q. Liu, X. Wang, P.A. Crozier, C.K. Chan, and R.J. Nemanich, *Al_2O_3 and SiO_2 Atomic Layer Deposition Layers on ZnO Photoanodes and Degradation Mechanisms.* ACS Applied Materials & Interfaces, 2017. **9**(19): p. 16138-16147.

15. Coppa, B.J., C.C. Fulton, P.J. Hartlieb, R.F. Davis, B.J. Rodriguez, B.J. Shields, and R.J. Nemanich, *In situ cleaning and characterization of oxygen- and zinc-terminated,n-type, ZnO{0001} surfaces.* Journal of Applied Physics, 2004. **95**(10): p. 5856-5864.

16. Brillson, L.J., *Transition in Schottky Barrier Formation with Chemical Reactivity.* Physical Review Letters, 1978. **40**(4): p. 260-263.

17. Brillson, L.J., H.L. Mosbacker, M.J. Hetzer, Y. Strzhemechny, G.H. Jessen, D.C. Look, G. Cantwell, J. Zhang, and J.J. Song, *Dominant effect of near-interface native point defects on ZnO Schottky barriers.* Applied Physics Letters, 2007. **90**(10): p. 102116.

18. Kohan, A.F., G. Ceder, D. Morgan, and C.G. Van de Walle, *First-principles study of native point defects in ZnO.* Physical Review B, 2000. **61**(22): p. 15019-15027.

19. Liu, L., Z. Mei, A. Tang, A. Azarov, A. Kuznetsov, Q.-K. Xue, and X. Du, *Oxygen vacancies: The origin of n-type conductivity in ZnO.* Physical Review B, 2016. **93**(23).

20. Allen, M.W., S.M. Durbin, and J.B. Metson, *Silver oxide Schottky contacts on n-type ZnO.* Applied Physics Letters, 2007. **91**(5): p. 053512.

21. Dong, Y., Z.Q. Fang, D.C. Look, G. Cantwell, J. Zhang, J.J. Song, and L.J. Brillson, *Zn- and O-face polarity effects at ZnO surfaces and metal interfaces.* Applied Physics Letters, 2008. **93**(7): p. 072111.

22. Kerkhof, F.P.J.M. and J.A. Moulijn, *Quantitative-Analysis of XPS Intensities for Supported Catalysts.* Journal of Physical Chemistry, 1979. **83**(12): p. 1612-1619.

23. Tanuma, S., C.J. Powell, and D.R. Penn, *Calculations of electron inelastic mean free paths. VIII. Data for 15 elemental solids over the 50-2000 eV range.* Surface and Interface Analysis, 2005. **37**(1): p. 1-14.

24. Powell, C.J. and A. Jablonski, *NIST Electron Inelastic-Mean-Free-Path Database - Version 1.2*. 2010: National Institute of Standards and Technology.

CHAPTER 5

PHOSPHORUS-DOPED DIAMOND GROWTH ON (100) SURFACES USING PULSE MODE DEPOSITION: PRETREATMENT EFFECTS AND BAND ALIGNMENT

5.1 Abstract

Diamond, as an ultra-wide bandgap semiconductor, has unique properties for solid-state and vacuum electronics. To enable devices, epitaxial growth of intrinsic and doped diamond layers is required, especially on (100) surfaces, which are becoming commercially available. Phosphorus has been considered as a candidate for n-type doping because of its donor level at ~0.6 eV below the conduction band. However, growth of P-doped diamond on (100) surfaces shows a low growth rate and inefficient dopant incorporation.

In this research, a pulse mode deposition method is employed to grow phosphorus-doped diamond layers on (100) single crystal diamond substrates. Different pretreatment conditions were employed prior to the growth. The results indicate that an initial O/H plasma process or a short H-plasma and CH_4/H_2 plasma process achieves an increased P-doped diamond growth rate. In addition, photoemission spectroscopy measurements were conducted for H-terminated diamond surfaces. Band alignment of the structures was deduced from the results. Moreover, Fermi level pinning effects were observed, which were independent of the doping. The pinning level, which is near the valence band maximum, is attributed to the diamond surface states and possible air adsorbate induced acceptor-like states.

(In collaboration with Franz A. Koeck, Yu Yang, Ernst Bauer and Robert J. Nemanich.)

5.2 Introduction

There is growing worldwide recognition that chemical vapor deposited (CVD) diamond materials will impact future high-power electronics. The properties of diamond that contribute to its value in power electronics include high electron and hole mobilities (>2000 cm^2/Vs), high breakdown field (10 MV/cm), highest thermal conductivity, and low dielectric constant [1]. Besides, as a group IV elemental semiconductor, problems associated with anti-site structural defects in III-V materials do not occur. Moreover, sp^3 bonded diamond has a single polytype, diamond cubic, which offers improved stability compared to other materials such as silicon carbide [1]. These properties enable diamond as an excellent material for high-power, high temperature and high-frequency electronic devices. To fabricate practical devices, high quality epitaxial diamond growth of intrinsic, p-type and n-type diamond must be achieved.

Naturally occurring n-type diamond has not been reported. Nitrogen, a common impurity in natural diamond, has a covalent bond length (0.74Å) that is similar to diamond (0.77Å), but due to a lattice distortion, N incorporation exhibits a deep donor level at ~1.7 eV below the conduction band minimum. Phosphorus has been considered as another candidate for n-type doping, which has shown an experimentally determined donor level of ~0.6 eV [2]. However, the large phosphorus covalent bond length (1.10 Å) results in difficulties during the incorporation process [3]. CVD phosphorus-doped diamond growth was initially achieved on (111) diamond surfaces [4]. Nevertheless, for practical applications, the growth of phosphorus-doped diamond on (100) surfaces is necessary. The (111) surface of diamond is noticeably harder to polish than the (100) surface, and a smooth and precisely oriented (111) surface is more difficult to achieve. Consequently, (111)

diamond plates cost more than (100) diamond substrates, and their size is limited. Thus, efficient pretreatment and growth methods for P-doped diamond film growth on (100) surfaces have become critical. In this study, P-doped diamond deposition was achieved by a pulse mode deposition method. To study the effects of the pretreatment for P-doped diamond (100) deposition, the growth process was kept consistent, and different pre-treatment conditions including 1) O/H plasma, 2) H-plasma and 3) CH_4/H_2 plasma were employed prior to the growth.

In addition, the surface states on H-terminated diamond surfaces are known to introduce band bending at diamond surface [5-7], which could influence properties such as thermionic emission. Measurements of the surface state level on H-terminated diamond can provide a guideline for diamond device design. Besides, the band alignment at the P-doped diamond/i-diamond interface provides fundamental understanding necessary for diamond devices. Thus, after obtaining the P-doped diamond growth on (100) diamond, photoemission spectroscopy (PES) was used to determine the band alignment of P-doped diamond/i-diamond interfaces.

5.3 Experiment

In this research, 4×4×0.5 mm optical grade IIa CVD (001) substrates were provided by Microwave Enterprises. Before transferring into a CVD system, the substrates were cleaned using the following chemical treatment: 1) boiled in an acid mixture (H_2SO_4:H_2O_2:H_2O, 3:1:1) at 220 ℃ for 15 minutes to remove organic and metallic contamination; 2) immersed in HF acid for 5 min at room temperature to remove SiO_2 and metallic contamination; and 3) boiled in SC1 (NH_4OH:H_2O_2:H_2O, 1:1:5) at 75℃ for 15

minutes to remove particles and organic contamination. After each chemical treatment, the substrates were rinsed with flowing deionized water. Samples were not re-polished, and the offcut angle of the samples was < 3 degrees.

Two microwave plasma-enhanced chemical vapor deposition (MPCVD) systems were employed for the sample pretreatment and growth processes. For sample pretreatment, three processes were employed. An O/H plasma (0.2% volume ratio, ~70 Torr, ~1200 W) process was used for surface cleaning/etching. A hydrogen plasma process operating at ~ 60 Torr, ~1500 W was used for *in-situ* substrate cleaning and plasma stabilization. A CH_4/H_2 plasma process with an ultra-low CH_4 concentration (0.05 % volume ratio) was employed to restore the bonding of the plasma cleaned surface. Various plasma process time lengths were employed for pretreatment effects investigation. The O/H plasma process was conducted in a re-engineered MPCVD reactor designed for intrinsic diamond growth. The microwave power was provided by an ASTeX 2.45 GHz source with a 1.8 kW maximum output power. The hydrogen plasma, CH_4/H_2 plasma and P-doped diamond growth were conducted in a separate MPCVD reactor designed for P-doped diamond growth with an ASTeX 2.45 GHz microwave source (5 kW maximum output power). Both MPCVD systems have a base pressure of $\sim 10^{-8}$ Torr through turbo molecular pumping. During the processes, the chambers are pumped by a four-stage, positive displacement rotary pump, and the chamber pressure is controlled by a butterfly valve.

After the pretreatment, 10 pulse cycles were applied to each of the samples in the above-mentioned 5 kW MPCVD system to compare the effects from different pretreatments. The deposition source gases were H_2, CH_4 and 200 parts per million (ppm) trimethylphosphine (TMP) diluted in H_2. Williamson dual-wavelength pyrometers were

employed during pretreatment and growth processes for *in-situ* measurements of the substrate temperature. An example substrate temperature vs time relation is plotted in FIG. 5.1.

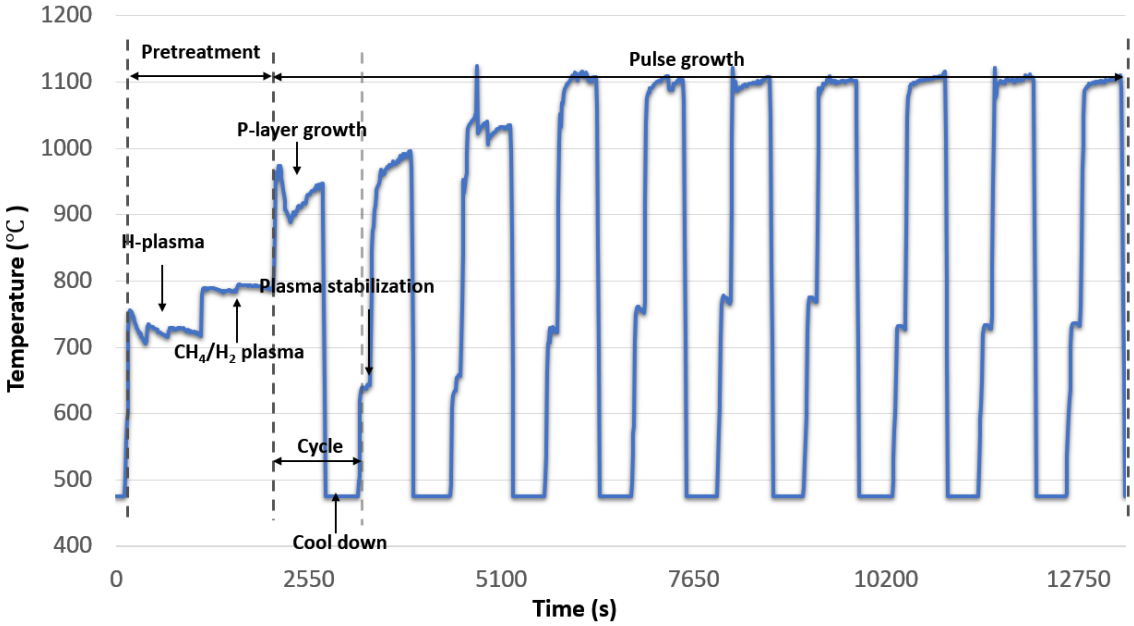

FIG. 5.1. Plot of typical substrate temperature vs time for phosphorus doped, n-type diamond growth on (100) using pulsed mode deposition method. (Low temperature value is limited by the pyrometer range.)

FIG. 5.1 shows temperature profile during a pretreatment of ~15 min H-plasma and ~15 min CH_4/H_2 plasma followed by the 10 pulse cycle growth process. Since these sample pretreatments were processed in the MPCVD system for P-doped diamond growth, 10 P-doped diamond growth cycles were conducted directly following the pretreatment. As shown in FIG. 5.1, each cycle consists of an ~8 min P-layer growth period with the plasma on and a ~5 min cooling time with plasma off. Since the sample is heated by the plasma, after the plasma was turned off, the substrate temperature decreases dramatically. The temperature during cooling periods is shown as 475 °C, which is the pyrometer lower

detection limit. However, the actual sample temperature could by lower than 475 °C. During the growth period with plasma on, samples reached a temperature of ~1050 °C. A microwave plasma power of ~2500 W was employed for the growth steps. The total gas flow rate was controlled to 400 standard cubic centimeters per minute (sccm) using mass flow controllers (MFC), including 2 sccm of CH_4, 10 sccm of TMP/H_2 and 388 sccm of H_2. The chamber pressure was keep at ~80 Torr.

An Olympus MX50L-R differential interference contrast (DIC) microscopy, an Asylum MFP-3D atomic force microscopy (AFM) operating in tapping mode and a prototype Elmitec LEEM III instrument operating at mirror electron microscopy (MEM) mode were employed for surface morphology characterization. A PANalytical X'Pert PRO MRD high resolution X-ray Diffractometer (XRD) was used for crystal misorientation characterization. Secondary ion mass spectrometry (SIMS) measurements using a Cs source was conducted by EAG Laboratories for film thickness and doping concentration analysis.

In addition, an integrated photoemission spectroscopy system was used for electronic band alignment measurements. The x-ray photoemission spectroscopy (XPS) system consists of a high intensity monochromatized Al K_α x-ray source (1486.7 eV) with a resolution of ~0.2 eV. The ultra-violet photoemission spectroscopy (UPS) systems is optimized for He I radiation at 21.2 eV. A Scienta R3000 high-resolution electron energy analyzer is employed to acquire spectra for both light sources. During the XPS measurement, a resolution of 0.1 eV was achieved, and the peak positions were determined using CasaXPS with an uncertainty of 0.05 eV. For UPS measurement, a bias of - 4.0 V was applied to the substrate to overcome the work function of the analyzer, and the analyzer

was operated at a 2 eV pass energy yielding a resolution of 3 meV. The photoemission system for both XPS and UPS was calibrated using a plasma cleaned gold foil.

A remote plasma system was employed for *in-situ* H-termination processes. During the remote H-plasma. The research-grade hydrogen flow rate was set to 30 sccm. The plasma was excited using RF power (13.56 MHz, 100 W) applied to a helical copper coil wrapped around a ~32 mm diameter quartz tube. The base of the quartz tube was ~200 mm away from the sample. The chamber pressure was set to 100 mTorr and the. Sample was heated to ~500 °C by a coil heater.

5.4 Pretreatment effects of P-doped diamond growth on (100) surface

5.4.1 Results

To understand the morphology change introduced by P-doped diamond film growth on a (100) surface and the correlation between growth rate and surface morphology, microscopies were employed for morphology analysis. Typical images before pretreatment and after P-doped diamond layer deposition obtained by the DIC microscopy, MEM and AFM are shown in FIG. 5.2. Before pretreatment, no obvious feature is observed in DIC image and an optically smooth surface is presented. AFM analysis indicated a RMS roughness between 1 ~ 7 nm for the IIa (100) substrates after the chemical cleaning process. Lines in the [100] direction are observed, which may be related to substrate polishing. It is worth to noting that at similar magnification as AFM, MEM image shows multiple waviness in the image. The waviness feature is presumed to originate from the substrate cutting and polishing process. The DIC microscopy and AFM images after pretreatment and P-doped layer growth are shown in FIG. 5.2 (d) and (e). Both DIC microscopy and

AFM images show evidence of surface waviness that occurs at an angle close to the [100] direction. It is possible that the waviness feature is related to the waviness feature observed in the MEM image before pretreatment. In the DIC microscopy image, non-epitaxial hillocks or particles were not observed in most samples. In the AFM image, some small features in the [110] direction were observed, which may suggest that a three-dimension random growth mechanism occurred on the surface, and no evidence shows that the growth is following step-flow growth mechanism. However, there was no obvious correlation between surface morphology features and the growth rate observed.

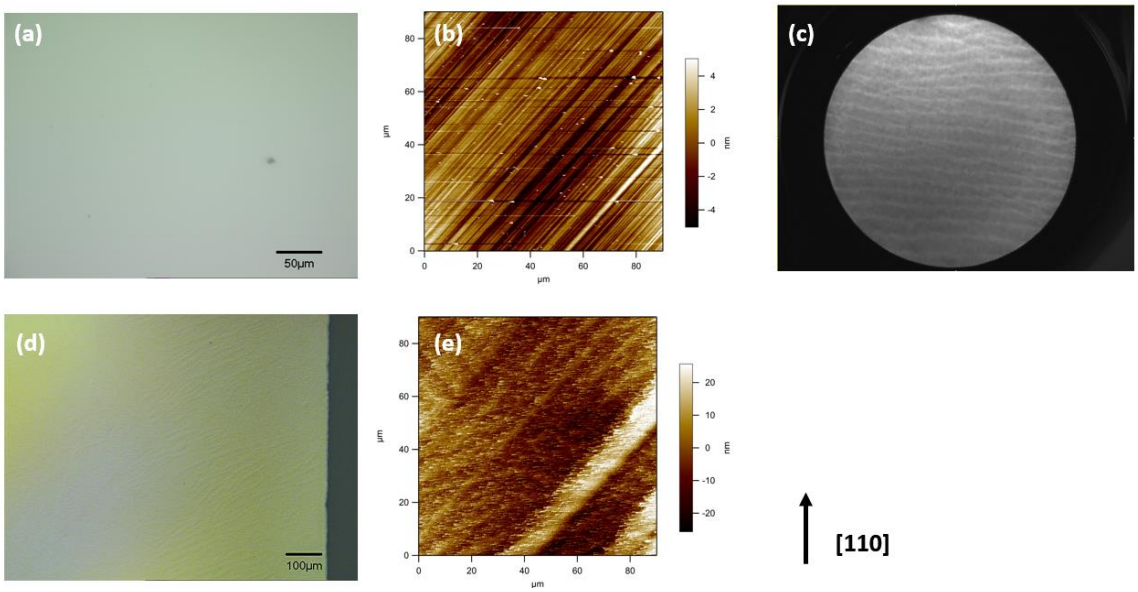

FIG. 5.2. Typical images of IIa diamond (100) substrates after chemical clean from: (a) DIC microscopy, (b) AFM and (c) MEM measurements and after P-doped film deposition from: (d) DIC microscopy and (e) AFM measurements. The lattice direction of the MEM image is unknown, and the [110] direction is indicated for other images.

Typical SIMS scans for phosphorus concentration are shown in FIG. 5.3. FIG. 5.3-(a) presents the doping profile of a representative film with a thickness of ~20 nm. FIG. 5.3-(b) presents scans from samples that show higher growth rate. FIG. 5.3-(c) presents

sample #17-026, which has the highest growth rate among all the samples obtained in this study. Since 10 deposition cycles were applied to each sample, growth rates of ~2 nm/cycle, ~10 nm/cycle and ~20 nm/cycle were deduced, respectively.

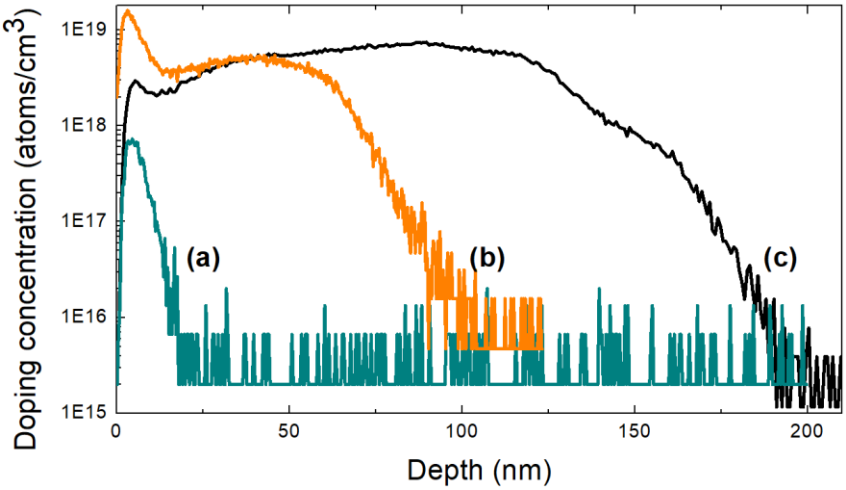

FIG. 5.3. SIMS doping profile for phosphorus doped diamond growth on (100) substrates, sample #: (a) 17-033, (b) 17-052, and (c) 17-026.

Sample misorientation angles, pretreatment time lengths, and post-growth results obtained from the AFM and SIMS measurements are summarized in TABLE 5.1. The misorientation angles were measured by XRD from bare substrates. The film thickness and P atoms doping concentration were deduced from SIMS results and RMS roughness was obtained by AFM analysis after the P-doped diamond film growth. From TABLE 5.1, it is evident that with the application of O/H plasma, a higher growth rate is obtained. In contrast, a H-plasma or CH_4/H_2 plasma process for more than an hour results in a reduced growth rate.

TABLE 5.1. A summary of sample misorientation angle, pretreatment time, P-doped film thickness, doping concentration and RMS roughness.

Sample #	Misorientation (°)	O/H plasma time (min)	H-plasma time (min)	CH_4/H_2 plasma time (min)	Thickness (nm)	P-doping concentration (atoms/cm^3)	RMS roughness (nm)
026	1.9	0	15	15	190	7E18	7
027	3.3	0	15	120	25	7E17	24
029	--	0	15	15	90	1E19	14
031	0.1	0	60	5	15	9E17	7
032	1.9	0	15	15	95	1E18	9
033	0.9	0	15	180	18	7E17	14
036	2.2	0	90	2	20	7E17	37
045	1.4	60	5	0	80	8E18	6
052	--	60	5	0	100	1E19	7

5.4.2 Discussion

Phosphorus-doped diamond growth on (100) surfaces is considerably more difficult than on (111) surfaces. It has been reported that the thermal stability of adsorbed phosphorus atoms on the (100) surface is reduced compared to the (111) surface, and the phosphorus atoms tend to segregate towards the surface especially on the (100) surface [3]. Because of the surface segregating tendency of P on (100) diamond, a high growth rate, which is faster than the phosphorus segregation velocity, is required [3]. Besides, on the diamond (100) surface, a phosphorus desorption time of 0.4 s was estimated based on experimental results [8], which is an order of magnitude less than the respective boron desorption time (used for p-type doping) [9].

As suggested above, a higher rate is necessary for P-doped diamond (100) growth, which requires a higher substrate temperature. However, this reduces the thermal stability of adsorbed phosphorus atoms. In this research, growth of phosphorus-doped diamond on the (100) surface was achieved by a pulse mode deposition method. With pulse mode deposition method, the cooling period provides a balance between high growth rate and lower temperature to increase surface adsorption.

Using data from TABLE 5.1, the relation between film thickness and misorientation angle is plotted in FIG. 5.4-(a), the relation between film thickness and after growth RMS roughness is shown in FIG. 5.4-(b), and the relation between P-doping density and thickness is shown in FIG. 5.4-(c).

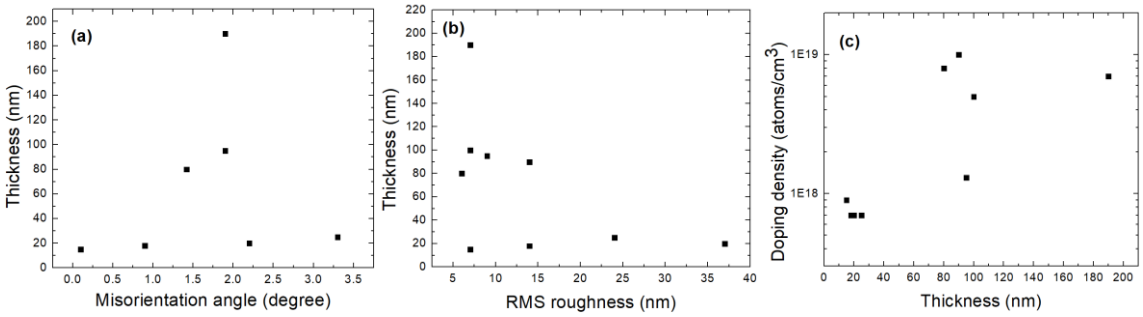

FIG. 5.4. Plots of (a) film thickness vs misorientation; (b) film thickness vs RMS roughness, and (c) doping concentration vs film thickness.

In previous reports, it has been suggested that with an increase of surface misorientation from the (100) surface, a higher growth rate is obtained for P-doped diamond [8]. However, as shown in FIG. 5.4-(a), with pulse mode deposition, no obvious positive correlation is observed. High misorientation angle may still result in very low growth rate compared to lower misorientation. The high growth rate samples typically have

misorientation angles in the range of 1° to 2°, which suggests that a vicinal (100) surface may still be important for P-doped diamond film growth.

In addition, a high concentration local hydrogen incorporation was reported on low misorientation angle samples, which causes non-epitaxial crystallites or hillocks on the surface along with a decreased film quality [3, 10]. As the example DIC microscopy image shows in FIG. 5.2-(d), non-epitaxial crystallite structure or hillocks did not appear on the surface. This suggests that the absence of high local hydrogen incorporation, which leads to an improved film quality.

It has been reported that a low surface roughness results in ~100% substitutional phosphorus incorporation [11], which is the preferred P atom incorporation structure [3]. FIG. 5.4-(b) shows the relation between surface roughness and film thickness. It is suggested that lower RMS roughness yields higher growth rate. AFM analysis indicated that after ~1-hour O/H plasma processes, low surface roughness of ~4 nm was mostly preserved. After P-doped film growth, a relatively low surface roughness is obtained, which may be related to the higher growth rate. In contrast, after a long pretreatment with H-plasma or CH_4/H_2 plasma, the P-doped film growth resulted in roughened surfaces, and a reduced growth rate was observed. As FIG. 5.4-(c) shows, when the film thickness is low, the doping concentration is relatively low, which may indicate that the difficulty of P atom incorporation also reduces the film thickness or growth rate.

5.5 Band alignment of P-doped diamond film on intrinsic diamond (100)

5.5.1 Results

XPS and UPS measurements were conducted on hydrogen terminated diamond (100) surfaces before and after P-doped film deposition. To understand the role of diamond (100) surface state and the air-exposure effects, the air-exposed H-terminated diamond samples were measured first. Then, remote H-plasma was employed to remove the air adsorbates and PES measurements were conducted again. The XPS carbon 1s peak scans are shown in FIG. 5.5. For air-exposed H-terminated surfaces, the C 1s peak was measured at 284.0 eV before deposition, which shifted to higher binding energy with increased thickness of P-doped diamond film. With the deposition of ~100 nm P-doped diamond film, the binding energy was 284.4 eV. For clean H-terminated surfaces, the situation is similar. Prior to the P-doped diamond film deposition, the C 1s peak was located at 284.2 eV. After ~100 nm P-doped diamond film deposition, the C 1s core level shifts to higher binding energy of 284.4 eV.

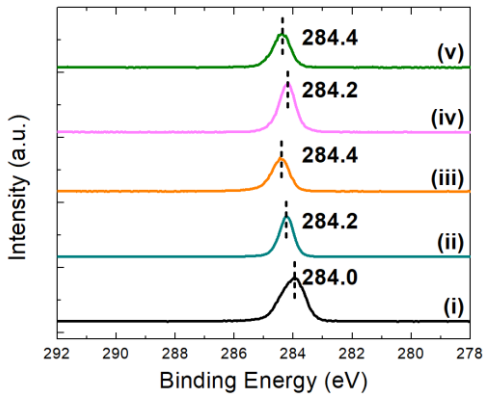

FIG. 5.5. XPS scans of the C 1s peaks for H-terminated air-exposed: (i) intrinsic diamond (100) surface, (ii) ~5 nm P-doped film on diamond (100) surface, (iii) ~100 nm P-doped film on diamond (100) surfaces, and clean H-terminated: (iv) intrinsic diamond (100) surface and (v) ~100 nm P-doped film on diamond (100) surface.

The UPS spectra for the H-terminated surfaces after air exposure are shown in FIG. 5.6. The VBM is measured to be 0.5 eV below the surface Fermi level for intrinsic diamond and ~5 nm P-doped diamond on diamond (100). For ~100 nm P-doped diamond film, the VBM is measured to be 0.7 eV below the surface Fermi level. The secondary peak edges of the UPS spectra are presented in FIG. 5.6-(b). The work function of the intrinsic diamond (100) surface and ~5 nm P-doped diamond film on intrinsic diamond (100) surface were indicated at 4.1 eV, and after ~100 nm P-doped diamond film deposition, the work function decreased to 3.8 eV.

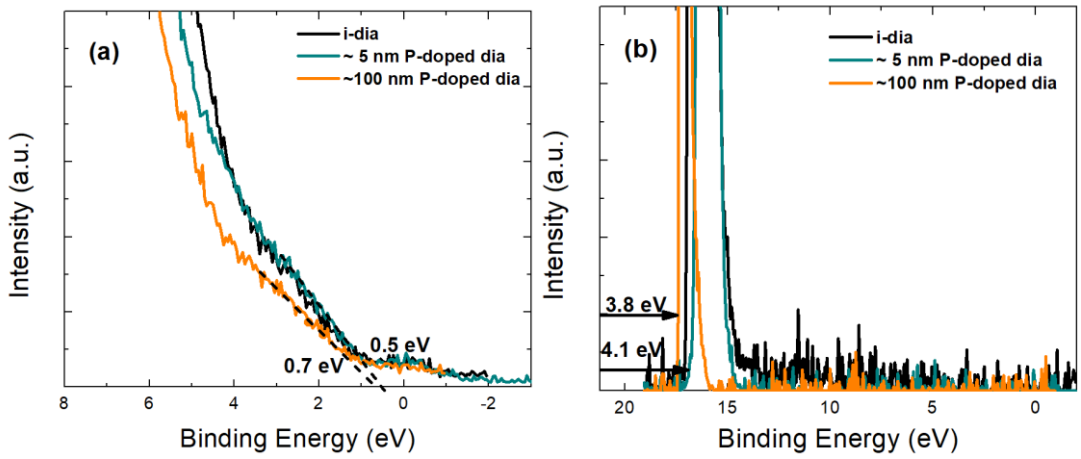

FIG. 5.6. UPS spectra for H-terminated air-exposed intrinsic diamond (100) surface, ~5 nm P-doped diamond film on intrinsic diamond (100) and ~100 nm P-doped diamond film on intrinsic diamond (100).

The electron affinity is calculated using the equation as follows [12]:

$$\chi = h\nu - E_g - W \qquad \text{Eq. (5.1)}$$

, where χ is the electron affinity, $h\nu$ is the photon energy (21.2 eV), E_g is the band gap of diamond (5.47 eV) and W is the width of the UPS spectra [2]. It is indicated that all three air-exposed H-terminated surfaces have negative electron affinities (NEA).

5.5.2 Discussion

The Fermi level of P-doped diamond was experimentally measured at 0.6 eV below the conduction band minimum (CBM) and the band gap of diamond is 5.47 eV [2, 4]. It was reported that when the Fermi level was located near the valence band maximum (VBM), the C 1s peak position was at 284.0 eV [13]. Thus, if the P-doped diamond film shows a flat band at the surface, a binding energy of 288.9 eV can be expected. However, according to our results, the binding energy is ~284.4 eV. Surface states, which behave like acceptors, have been suggested to exist on diamond surfaces with and without air-exposure [6]. In addition, the air adsorbates could also introduce electronic states [14]. A surface transfer doping model has been proposed previously to explain the surface conductivity of air exposed H-terminated diamond surface [14, 15].

For non-air-exposed H-terminated intrinsic diamond (100) surface, the XPS C 1s binding energy was measured at 284.2 eV. After ~100 nm P-doped diamond film deposition, the binding energy only increased 0.2 eV to 284.4 eV. For air-exposed H-terminated surfaces, the XPS C 1s core level was determined at 284.0 eV before P-doped film deposition, which indicates that the Fermi level was aligned near the VBM of the intrinsic diamond surface. The VBM was measured at 0.2 eV and 0.4 eV below the Fermi level after ~5 nm and ~100 nm P-doped diamond film growth, respectively. The results suggest that the C 1s core level positions were not affected strongly by the P-doped diamond film deposition or air-exposure. Band diagrams deduced from the XPS measurements are presented in FIG. 5.7.

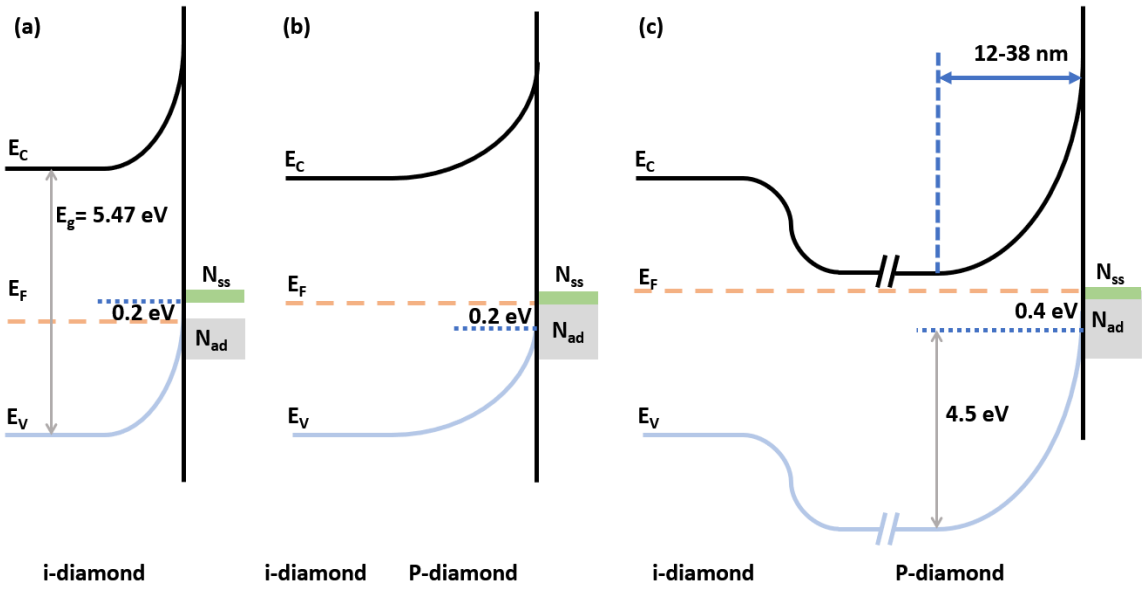

FIG. 5.7. Band alignment of H-terminated air-exposed (a) intrinsic diamond (100) surface; (b) ~5 nm P-doped diamond film on intrinsic diamond (100); and (c) ~100 nm P-doped diamond film on intrinsic diamond (100).

It has been reported that the surface states have acceptor-like behavior [6]. From XPS results on clean H-terminated diamond, we can see that the Fermi level is pinned at ~0.3 eV above VBM, which indicates the surface states level on the clean H-terminated diamond (100) surface. Before P-doped film deposition, the Fermi level is measured at 0.2 eV above the VBM, which shows the lower edge of the surface states. After P-doped diamond film deposition, since P atoms can provide electrons, which partially fill the surface states, thus the binding energy increases slightly by 0.2 eV.

For the air-exposed H-terminated diamond surface, a previous study from our group shows that the C 1s peak was at 284.0 eV for H-terminated boron-doped diamond surface after air exposure. Similarly, according to the results from intrinsic diamond, P-doped diamond, and the previous result for B-doped diamond, all the XPS C 1s results are close

to 284.0 eV indicating a Fermi level pinning effect for intrinsic, n-type and p-type diamond surfaces. Air adsorbate induced electronic states were proposed in diamond surface transfer doping model, which have acceptor-like behavior [14, 15]. The Fermi level pinning effect can be attribute to these electronic states. According to our measurements, the adsorbate introduced electronic states are close to or below the diamond VBM on H-terminated surface, which is a slightly lower energy level compared to the surface states. Both type of surface states can enable electron transfer from diamond to the acceptor-like electronic states, which results in upward band bending, until the surface Fermi level is aligned with the states.

Poisson's equation can be used to calculate the depletion region width [16]:

$$\Delta\phi = \frac{\rho d^2}{\varepsilon\varepsilon_0} \qquad \text{Eq. (5.2)}$$

, where $\Delta\phi$ is the potential change (~4.5 V measured by XPS), ρ is the charge density determined by P-doping concentration (~10^{18} to 10^{19} atoms/cm^3 measured by SIMS), d is the depletion region width, ε is the diamond dielectric constant (5.7) and ε_0 is the vacuum permittivity [17]. Based on Poisson's equation, depletion region widths of 38 and 12 nm are obtained for the doping concentrations of 10^{18} and 10^{19} atoms/cm^3, respectively.

No obvious C 1s shoulder peak is observed for air exposed H-terminated ~5 nm P-doped diamond/i-diamond interface. A reason is that the depletion region is suggested to be greater than the thickness of the P-doped diamond film. This depletion region eliminates the intrinsic and P-doped diamond interface effects. In addition, since SIMS results show that the phosphorus atoms incorporation increases gradually with the film growth, this contributes to a diffused interface behavior. After a thicker P-doped film was deposited, the depletion region between intrinsic and P-doped diamond layer appeared. At the surface,

the adsorbate and surface states cause a strong upward band bending of ~4.5 eV. The slight increase of binding energy after ~5 nm and ~100 nm P-doped diamond film deposition can be attributed to the electrons provided by phosphorus donor partially filling up the adsorbate introduced states and the intrinsic surface states.

The UPS results indicate a negative electron affinity (NEA) on all three surfaces, which is consistent with other reports [5, 18]. However, the VBM values provided by UPS measurements are inconsistent with results deduced from XPS measurements. This might be attributed to the fact that the UPS signal is detected close to the Fermi level, which makes the VBM signal unclear and results inaccurate. In addition, the measurement depth difference may also contribute to the discrepancy.

5.6 Conclusion

In this research, P-doped diamond film growth was successfully achieved by pulse mode deposition method. Various pretreatments including hydrogen plasma, CH_4/H_2 plasma and O/H plasma were applied to the samples. A short period of H-plasma, CH_4/H_2 plasma process or a long period of O/H plasma process results in higher growth rate. The results do not show a direct correlation between growth rate and substrate misorientation. However, it is suggested that a lower surface roughness is related to a higher growth rate.

PES measurements were conducted on H-terminated diamond surfaces before and after P-doped deposition. Fermi pinning effects were observed, which is attributed to the diamond surface states and the air adsorbate induced states. The lower edge of the diamond surface state is determined to be 0.2 eV above the VBM and the air adsorbate induced states are located slightly lower. The slightly increased C 1s core level binding energy after P-

doped film growth is related to electrons from the P donors filling up the states. In addition, NEA are suggested by UPS measurements for all H-terminated surfaces.

Acknowledgments

This research supported by Microwave Enterprise Ltd.

References:

1. Tsao, J.Y., S. Chowdhury, M.A. Hollis, D. Jena, N.M. Johnson, K.A. Jones, R.J. Kaplar, S. Rajan, C.G. Van de Walle, E. Bellotti, C.L. Chua, R. Collazo, M.E. Coltrin, J.A. Cooper, K.R. Evans, S. Graham, T.A. Grotjohn, E.R. Heller, M. Higashiwaki, M.S. Islam, P.W. Juodawlkis, M.A. Khan, A.D. Koehler, J.H. Leach, U.K. Mishra, R.J. Nemanich, R.C.N. Pilawa-Podgurski, J.B. Shealy, Z. Sitar, M.J. Tadjer, A.F. Witulski, M. Wraback, and J.A. Simmons, *Ultrawide-Bandgap Semiconductors: Research Opportunities and Challenges.* Advanced Electronic Materials, 2018. **4**(1): p. 1600501.

2. Kato, H., W. Futako, S. Yamasaki, and H. Okushi, *Homoepitaxial growth and characterization of phosphorus-doped diamond using tertiarybutylphosphine as a doping source.* Diamond and Related Materials, 2004. **13**(11-12): p. 2117-2120.

3. Kato, H., T. Makino, S. Yamasaki, and H. Okushi, *N-type diamond growth by phosphorus doping on (001)-oriented surface.* Journal of Physics D: Applied Physics, 2007. **40**(20): p. 6189-6200.

4. Koizumi, S., M. Kamo, Y. Sato, H. Ozaki, and T. Inuzuka, *Growth and characterization of phosphorous doped {111} homoepitaxial diamond thin films.* Applied Physics Letters, 1997. **71**(8): p. 1065-1067.

5. Koeck, F.A.M. and R.J. Nemanich, *Advances in Thermionic Energy Conversion through Single-Crystal n-Type Diamond.* Frontiers in Mechanical Engineering, 2017. **3**.

6. Kono, S., T. Nohara, S. Abe, H. Kodama, K. Suzuki, S. Koizumi, T. Abukawa, and A. Sawabe, *Electron Spectroscopic Determination of Electronic Structures of Phosphorus-Doped n-Type Heteroepitaxial Diamond (001) Surface and Junction.* Japanese Journal of Applied Physics, 2012. **51**: p. 090109.

7. Suzuki, M., S. Koizumi, M. Katagiri, T. Ono, N. Sakuma, H. Yoshida, T. Sakai, and S. Uchikoga, *Electrical characteristics of n-type diamond Schottky diodes and metal/diamond interfaces.* physica status solidi (a), 2006. **203**(12): p. 3128-3135.

8. Kawashima, H., H. Kato, M. Ogura, D. Takeuchi, T. Makino, and S. Yamasaki, *Desorption time of phosphorus during MPCVD growth of n-type (001) diamond.* Diamond and Related Materials, 2016. **64**: p. 208-212.

9. Ogura, M., H. Kato, T. Makino, H. Okushi, and S. Yamasaki, *Misorientation-angle dependence of boron incorporation into (001)-oriented chemical-vapor-deposited (CVD) diamond.* Journal of Crystal Growth, 2011. **317**(1): p. 60-63.

10. Pinault-Thaury, M.A., T. Tillocher, D. Kobor, N. Habka, F. Jomard, J. Chevallier, and J. Barjon, *Phosphorus donor incorporation in (100) homoepitaxial diamond: Role of the lateral growth.* Journal of Crystal Growth, 2011. **335**(1): p. 31-36.

11. Pinault-Thaury, M.A., B. Berini, I. Stenger, E. Chikoidze, A. Lusson, F. Jomard, J. Chevallier, and J. Barjon, *High fraction of substitutional phosphorus in a (100) diamond epilayer with low surface roughness.* Applied Physics Letters, 2012. **100**(19): p. 192109.

12. Nemanich, R.J., P.K. Baumann, M.C. Benjamin, O.H. Nam, A.T. Sowers, B.L. Ward, H. Ade, and R.F. Davis, *Electron emission properties of crystalline diamond and III-nitride surfaces.* Applied Surface Science, 1998. **130-132**: p. 694-703.

13. Yang, Y., F.A. Koeck, M. Dutta, X. Wang, S. Chowdhury, and R.J. Nemanich, *Al_2O_3 dielectric layers on H-terminated diamond: Controlling surface conductivity.* Journal of Applied Physics, 2017. **122**(15): p. 155304.

14. Maier, F., M. Riedel, B. Mantel, J. Ristein, and L. Ley, *Origin of Surface Conductivity in Diamond.* Physical Review Letters, 2000. **85**(16): p. 3472-3475.

15. Takeuchi, D., M. Riedel, J. Ristein, and L. Ley, *Surface band bending and surface conductivity of hydrogenated diamond.* Physical Review B, 2003. **68**(4).

16. Xi, S., W. Jie, G. Zha, Y. Yuan, T. Wang, W. Zhang, J. Zhu, L. Xu, Y. Xu, J. Su, H. Zhang, Y. Gu, J. Li, J. Ren, and Q. Zhao, *Effects of Ga-Te interface layer on the potential barrier height of CdTe/GaAs heterointerface.* Phys. Chem. Chem. Phys., 2016. **18**(4): p. 2639-2645.

17. Bhagavantam, S. and D.A.A.S. Narayana Rao, *Dielectric Constant of Diamond.* Nature, 1948. **161**(4097): p. 729-729.

18. Yamada, T., T. Masuzawa, H. Mimura, and K. Okano, *Electron emission from conduction band of heavily phosphorus doped diamond negative electron affinity surface.* Journal of Physics D: Applied Physics, 2016. **49**(4): p. 045102.

CHAPTER 6

CONCLUSIONS AND FUTURE WORK

6.1 Conclusions of Work

The research in this dissertation focuses on *in-situ* photoemission spectroscopy (PES) characterization at semiconductor interfaces, where effects due to interface electronic states were observed. The results can be summarized as follows:

The CdTe/InSb (100) heterojunction grown by molecular beam epitaxial (MBE) was employed as a model heterojunction between II-VI and III-V materials. Because of the small lattice mismatch, the CdTe/InSb (100) heterojunction provides an opportunity for studying electronic state effects introduced from non-octal chemical bonding without interference from other lattice effects. Hydrogen plasma was utilized before *in-situ* PES measurements for surface contamination removal. According to x-ray photoemission spectroscopy (XPS) measurements, surface contamination was removed by H-plasma and the sample stoichiometry was preserved. Combined with ultra-violet photoemission spectroscopy (UPS) results, a type-I (staggered type) band alignment was observed at the heterointerface. A valence band offset of 0.89 eV was deduced. A ~1.5 nm thick interface layer containing In-Te bonding is suggested from the XPS results. We proposed that the chemical bonds between group III and group VI material provide free electrons, which leads to a donor like behavior. The free electrons accumulate at the InSb side of the interface, and consequently cause downward band bending.

Cu/ZnO interfaces were employed for the study of the electronic states at metal interfaces on polar material. Photoemission spectroscopy measurements indicate ohmic

behavior at Cu/ZnO $(000\bar{1})$ and Cu/polycrystalline ZnO deposited by plasma-enhance atomic layer deposition (PEALD). In contrast, a 0.3 eV Schottky barrier was measured at the Cu/ZnO (0001) interface. XPS results indicate the formation of a copper-oxygen interface layer, which may lead to the formation of oxygen vacancies in the ZnO. The donor behavior of oxygen vacancies can provide free electrons, which would diffuse into bulk ZnO and form a depletion region. This would cause downward band bending and a lower barrier height. The lower barrier height at the Cu/ZnO $(000\bar{1})$ interface is proposed to be caused by a larger concentration of oxygen vacancies in the ZnO compared to the Cu/ZnO (0001) interface. PEALD ZnO was intentionally introduced to observe the effects of a reduced polarization due to the random orientation. However, other effects of the polycrystalline structure are suspected to be introduced, which could contribute to the observed ohmic behavior.

H-terminated P-doped diamond/intrinsic diamond (100) interfaces were introduced for diamond band alignment study. The P-doped diamond films were prepared by a pulse mode deposition method using microwave plasma-enhanced chemical vapor deposition (MPCVD). First, the pretreatment effects for P-doped diamond (100) film growth were characterized. It is suggested that an O/H plasma treatment or a short period of H-plasma and CH_4/H_2 plasma results in a high growth rate. It is proposed that a low surface roughness is important for a high growth rate. PES was applied for electronic states measurements. Combined with results from a previous study, Fermi level pinning effects were observed, which were independent of the doping properties. The Fermi level pinning effect is attributed to surface states and air adsorbate introduced electronic states, which show

acceptor-like behavior. According to XPS results, the electronic states are located near the valence band maximum (VBM) of diamond.

6.2 Outline of Future Work

Since the electronic states of semiconductor interfaces are sensitive to many factors and difficult to predict, PES is always an effective technique for electronic states measurements. Here interesting topics are presented in areas that are closely related to the projects in this dissertation.

The electronic states at MPCVD grown H-terminated P-doped diamond surfaces, and P-doped diamond/intrinsic diamond (100) interfaces were studied in this dissertation. The ultra-violet photoemission spectroscopy (UPS) signal close to the Fermi level directly may suggest the presence of surface states and air adsorbate induced electronic states. However, during the experiment, He I radiation was applied, and the He I β line at 23.1 eV might also contribute to the signal near the Fermi level, which makes the origin of the signal unclear. Thus, to confirm the observation of the electronic states close to the VBM more clearly, He II radiation (40.8 eV) can be employed.

In addition, the same method could be utilized to measure the surface states position on clean hydrogen terminated diamond surfaces at different temperature [1]. The negative electron affinity (NEA) property of an H-terminated diamond surface makes it a promising material for thermionic emission applications [2]. However, the surface states location for clean hydrogen terminated diamond may significantly affect the diamond thermionic emission behavior [3]. Thus, using PES to measure the surface states becomes interesting, especially at different temperatures. MPCVD deposition could be used for intrinsic, p-type

and n-type diamond (100) growth. *In-situ* hydrogen plasma could be employed for air-contamination removal and H-termination. Then, *in-situ* photoemission spectroscopy will be applied for characterization of the surface states on the clean H-terminated surfaces. With the usage of intrinsic, p-type and n-type diamond (100), the energy level of the surface states can be deduced from the PES measurements. In addition, if high doping concentration P-doped layer could be achieved, a flat band with the electronic states fulfilled can be expected. Besides, since the energy level of the surface states are supposed to be higher than the adsorbate introduced states mentioned in this dissertation, the UPS could show more distinguishable signal from the electronic states.

The pulse mode deposition method for P-doped diamond growth on diamond (100) still needs to be understood more comprehensively. Although the P-doped diamond (100) deposition can be achieved now, many questions need to be answered. For example, is the film thickness is linear to the applied growth cycle number? There might be a limiting factor for the P-doped diamond (100) growth, which might stop the growth suddenly. In addition, as we see in this dissertation, the P-doping concentration gradually increases with the P-doped diamond deposition, which results in a blurry interface. A method to improve the interface doping concentration could be important for better interface quality. To answer these questions, more experiments need to be conducted. By knowing these answers, we could understand the physical properties of the growth mechanism, which should help with improving the deposition process and film quality significantly.

References

1. Graupner, R., M. Hollering, A. Ziegler, J. Ristein, L. Ley, and A. Stampfl, *Dispersions of surface states on diamond (100) and (111)*. Physical Review B, 1997. 55(16): p. 10841-10847.

2. Koeck, F.A.M., R.J. Nemanich, A. Lazea, and K. Haenen, *Thermionic electron emission from low work-function phosphorus doped diamond films*. Diamond and Related Materials, 2009. 18(5-8): p. 789-791.

3. Koeck, F.A.M. and R.J. Nemanich, *Advances in Thermionic Energy Conversion through Single-Crystal n-Type Diamond*. Frontiers in Mechanical Engineering, 2017. 3.

REFERENCES

The Nobel Prize in Physics 2000. 2000; Available from: http://www.nobelprize.org/nobel_prizes/physics/laureates/2000/.

Franciosi, A. and C.G. Van de Walle, *Heterojunction band offset engineering.* Surface Science Reports, 1996. **25**(1-4): p. 1-140.

Lüth, H., *Solid surfaces, interfaces and thin films*. 4th, rev. and extended ed. 2001, Berlin ; New York: Springer. xiii, 559 p.

Forstmann, F., *The concepts of surface states.* Progress in Surface Science, 1993. **42**(1-4): p. 21-31.

Shockley, W., *On the Surface States Associated with a Periodic Potential.* Physical Review, 1939. **56**(4): p. 317-323.

Tamm, I., *On the possible bound states of electrons on a crystal surface.* Phys. Z. Soviet Union, 1932(1): p. 733.

Müller, G., A. Friedberger, and K. Knese, *Porous Silicon Based MEMS.* 2015: p. 503-524.

Mönch, W., *Barrier heights of real Schottky contacts explained by metal-induced gap states and lateral inhomogeneities.* Journal of Vacuum Science & Technology B: Microelectronics and Nanometer Structures, 1999. **17**(4): p. 1867.

Nishimura, T., K. Kita, and A. Toriumi, *Evidence for strong Fermi-level pinning due to metal-induced gap states at metal/germanium interface.* Applied Physics Letters, 2007. **91**(12): p. 123123.

Tejedor, C., F. Flores, and E. Louis, *The metal-semiconductor interface: Si (111) and zincblende (110) junctions.* Journal of Physics C: Solid State Physics, 1977. **10**(12): p. 2163-2177.

Heine, V., *Theory of Surface States.* Physical Review, 1965. **138**(6A): p. A1689-A1696.

Farrell, H.H., M.C. Tamargo, J.L. de Miguel, F.S. Turco, D.M. Hwang, and R.E. Nahory, *"Designer" interfaces in II-VI/III-V polar heteroepitaxy*. Journal of Applied Physics, 1991. **69**(10): p. 7021-7028.

Harrison, W.A., E.A. Kraut, J.R. Waldrop, and R.W. Grant, *Polar heterojunction interfaces.* Physical Review B, 1978. **18**(8): p. 4402-4410.

Xi, S., W. Jie, G. Zha, Y. Yuan, T. Wang, W. Zhang, J. Zhu, L. Xu, Y. Xu, J. Su, H. Zhang, Y. Gu, J. Li, J. Ren, and Q. Zhao, *Effects of Ga-Te interface layer on the potential barrier height of CdTe/GaAs heterointerface.* Phys. Chem. Chem. Phys., 2016. **18**(4): p. 2639-2645.

Frey, A., U. Bass, S. Mahapatra, C. Schumacher, J. Geurts, and K. Brunner, *Band offsets and band bending at heterovalent semiconductor interfaces.* Physical Review B, 2010. **82**(19).

Janotti, A. and C.G. Van de Walle, *Fundamentals of zinc oxide as a semiconductor.* Reports on Progress in Physics, 2009. **72**(12): p. 126501.

Janotti, A. and C.G. Van de Walle, *New insights into the role of native point defects in ZnO.* Journal of Crystal Growth, 2006. **287**(1): p. 58-65.

Janotti, A. and C.G. Van de Walle, *Oxygen vacancies in ZnO.* Applied Physics Letters, 2005. **87**(12): p. 122102.

Liu, L., Z. Mei, A. Tang, A. Azarov, A. Kuznetsov, Q.-K. Xue, and X. Du, *Oxygen vacancies: The origin of n-type conductivity in ZnO.* Physical Review B, 2016. **93**(23).

Zangwill, A., *Physics at surfaces*. 1988: Cambridge University Press.

Hüfner, S., *Photoelectron Spectroscopy Principles and Applications. 3 ed.* 2003: Springer-Verlag Berlin Heidelberg.

Lim, S.J., S. Kwon, and H. Kim, *ZnO thin films prepared by atomic layer deposition and rf sputtering as an active layer for thin film transistor.* Thin Solid Films, 2008. 516(7): p. 1523-1528.

Wójcik, A., M. Godlewski, E. Guziewicz, R. Minikayev, and W. Paszkowicz, *Controlling of preferential growth mode of ZnO thin films grown by atomic layer deposition.* Journal of Crystal Growth, 2008. 310(2): p. 284-289.

Lujala, V., J. Skarp, M. Tammenmaa, and T. Suntola, *Atomic layer epitaxy growth of doped zinc oxide thin films from organometals.* Applied Surface Science, 1994. 82-83: p. 34-40.

Nassau, K. and J. Nassau, *The history and present status of synthetic diamond.* Journal of Crystal Growth, 1979. 46(2): p. 157-172.

Kato, H., T. Makino, S. Yamasaki, and H. Okushi, *N-type diamond growth by phosphorus doping on (001)-oriented surface.* Journal of Physics D: Applied Physics, 2007. 40(20): p. 6189-6200.

Gracio, J.J., Q.H. Fan, and J.C. Madaleno, *Diamond growth by chemical vapour deposition.* Journal of Physics D: Applied Physics, 2010. 43(37): p. 374017.

Waldrop, J.R. and R.W. Grant, *Measurement of AlN/GaN (0001) heterojunction band offsets by x-ray photoemission spectroscopy.* Applied Physics Letters, 1996. 68(20): p. 2879-2881.

Coppa, B.J., C.C. Fulton, S.M. Kiesel, R.F. Davis, C. Pandarinath, J.E. Burnette, R.J. Nemanich, and D.J. Smith, *Structural, microstructural, and electrical properties of gold films and Schottky contacts on remote plasma-cleaned, n-type ZnO{0001} surfaces.* Journal of Applied Physics, 2005. 97(10): p. 103517.

Kraut, E.A., R.W. Grant, J.R. Waldrop, and S.P. Kowalczyk, *Precise Determination of the Valence-Band Edge in X-Ray Photoemission Spectra: Application to Measurement of Semiconductor Interface Potentials.* Physical Review Letters, 1980. 44(24): p. 1620-1623.

Waldrop, J.R., E.A. Kraut, S.P. Kowalczyk, and R.W. Grant, *Valence-band discontinuities for abrupt (110), (100), and (111) oriented Ge-GaAs heterojunctions.* Surface Science, 1983. 132(1-3): p. 513-518.

Waldrop, J.R. and R.W. Grant, *Semiconductor Heterojunction Interfaces: Nontransitivity of Energy-band Discontiuities*. 1988. 1: p. 287-290.

Wang, X., C. Campbell, Y.-H. Zhang, and R.J. Nemanich, *Band alignment at the CdTe/InSb (001) heterointerface.* Journal of Vacuum Science and Technology, A, 2018. 36: p. 031101.

Kerkhof, F.P.J.M. and J.A. Moulijn, *Quantitative-Analysis of XPS Intensities for Supported Catalysts.* Journal of Physical Chemistry, 1979. 83(12): p. 1612-1619.

Dandrea, R.G., S. Froyen, and A. Zunger, *Stability and band offsets of heterovalent superlattices: Si/GaP, Ge/GaAs, and Si/GaAs.* Physical Review B, 1990. 42(5): p. 3213-3216.

Farrow, R.F.C., G.R. Jones, G.M. Williams, and I.M. Young, *Molecular beam epitaxial growth of high structural perfection, heteroepitaxial CdTe films on InSb (001).* Applied Physics Letters, 1981. 39(12): p. 954-956.

Mackey, K.J., P.M.G. Allen, W.G. Herrenden-Harker, R.H. Williams, C.R. Whitehouse, and G.M. Williams, *Chemical and electronic structure of InSb-CdTe interfaces.* Applied Physics Letters, 1986. 49(6): p. 354-356.

Lu, J., M.J. DiNezza, X.-H. Zhao, S. Liu, Y.-H. Zhang, A. Kovacs, R.E. Dunin-Borkowski, and D.J. Smith, *Towards defect-free epitaxial CdTe and MgCdTe layers grown on InSb (001) substrates.* Journal of Crystal Growth, 2016. 439: p. 99-103.

Zhao, X.-H., M.J. DiNezza, S. Liu, C.M. Campbell, Y. Zhao, and Y.-H. Zhang, *Determination of CdTe bulk carrier lifetime and interface recombination velocity of*

CdTe/MgCdTe double heterostructures grown by molecular beam epitaxy. Applied Physics Letters, 2014. 105(25): p. 252101.

Zhao, Y., M. Boccard, S. Liu, J. Becker, X.-H. Zhao, C.M. Campbell, E. Suarez, M.B. Lassise, Z. Holman, and Y.-H. Zhang, *Monocrystalline CdTe solar cells with open-circuit voltage over 1 V and efficiency of 17%.* Nature Energy, 2016. 1(6): p. 16067.

Bell, G.R., N.S. Kaijaks, R.J. Dixon, and C.F. McConville, *Atomic hydrogen cleaning of polar III-V semiconductor surfaces.* Surface Science, 1998. 401(2): p. 125-137.

Jaime-Vasquez, M., M. Martinka, A.J. Stoltz, R.N. Jacobs, J.D. Benson, L.A. Almeida, and J.K. Markunas, *Plasma-Cleaned InSb (112)B for Large-Area Epitaxy of HgCdTe Sensors.* Journal of Electronic Materials, 2008. 37(9): p. 1247-1254.

Fonthal, G., L. Tirado-Mejía, J.I. Marín-Hurtado, H. Ariza-Calderón, and J.G. Mendoza-Alvarez, *Temperature dependence of the band gap energy of crystalline CdTe.* Journal of Physics and Chemistry of Solids, 2000. 61(4): p. 579-583.

Littler, C.L. and D.G. Seiler, *Temperature dependence of the energy gap of InSb using nonlinear optical techniques*. Applied Physics Letters, 1985. 46(10): p. 986-988.

Stariy, S.V., A.V. Sukach, V.V. Tetyorkin, V.O. Yukhymchuk, and T.R. Stara, *Effect of thermal annealing on electrical and photoelectrical properties of n-InSb.* Semiconductor Physics Quantum Electronics and Optoelectronics, 2017. 20(1): p. 105-109.

Liu, J. and T. Zhang, *Rapid thermal annealing characteristics of Be implanted into InSb.* Applied Surface Science, 1998. 126(3-4): p. 231-234.

Tanuma, S., C.J. Powell, and D.R. Penn, *Calculations of electron inelastic mean free paths. VIII. Data for 15 elemental solids over the 50-2000 eV range*. Surface and Interface Analysis, 2005. 37(1): p. 1-14.

Powell, C.J. and A. Jablonski, *NIST Electron Inelastic-Mean-Free-Path Database - Version 1.2*. 2010: National Institute of Standards and Technology.

Waldrop, J.R. and R.W. Grant, *Semiconductor Heterojunction Interfaces: Nontransitivity of Energy-band Discontinuities*. Physical Review Letters, 1979. 43(22): p. 1686-1689.

Reynolds, D.C. and T.C. Collins, *Excited Terminal States of a Bound Exciton-Donor Complex in ZnO.* Physical Review, 1969. **185**(3): p. 1099-1103.

Thomas, D.G., *The exciton spectrum of zinc oxide.* Journal of Physics and Chemistry of Solids, 1960. **15**(1-2): p. 86-96.

Look, D.C., *Recent advances in ZnO materials and devices.* Materials Science and Engineering: B, 2001. **80**(1-3): p. 383-387.

Brillson, L.J. and Y. Lu, *ZnO Schottky barriers and Ohmic contacts.* Journal of Applied Physics, 2011. **109**(12): p. 121301.

Jacobi, K., G. Zwicker, and A. Gutmann, *Work function, electron affinity and band bending of zinc oxide surfaces.* Surface Science, 1984. **141**(1): p. 109-125.

Kohl, D., M. Henzler, and G. Heiland, *Low temperature sublimation processes from clean cleaved polar surfaces of zinc oxide crystals during first heating.* Surface Science, 1974. **41**(2): p. 403-411.

Göpel, W., L.J. Brillson, and C.F. Brucker, *Surface point defects and Schottky barrier formation on ZnO(10$\bar{1}$0).* Journal of Vacuum Science and Technology, 1980. **17**(5): p. 894-898.

Sze, S.M. and K.K. Ng, *Physics of Semiconductor Devices*. 2006, New York: Wiley.

Zúñiga-Pérez, J., V. Consonni, L. Lymperakis, X. Kong, A. Trampert, S. Fernández-Garrido, O. Brandt, H. Renevier, S. Keller, K. Hestroffer, M.R. Wagner, J.S. Reparaz, F. Akyol, S. Rajan, S. Rennesson, T. Palacios, and G. Feuillet, *Polarity in GaN and ZnO: Theory, measurement, growth, and devices.* Applied Physics Reviews, 2016. **3**(4): p. 041303.

Kattel, S., P.J. Ramírez, J.G. Chen, J.A. Rodriguez, and P. Liu, *Active sites for CO_2 hydrogenation to methanol on Cu/ZnO catalysts.* Science, 2017. **355**(6331): p. 1296-1299.

Benipal, M.K., *Photoinduced Charge Transfer at Metal Oxide/Oxide Interfaces Prepared with Plasma Enhanced Atomic Layer Deposition*. 2016, Arizona State University. p. 242.

Cheng, Q., M.K. Benipal, Q. Liu, X. Wang, P.A. Crozier, C.K. Chan, and R.J. Nemanich, *Al_2O_3 and SiO2 Atomic Layer Deposition Layers on ZnO Photoanodes and Degradation Mechanisms.* ACS Applied Materials & Interfaces, 2017. **9**(19): p. 16138-16147.

Coppa, B.J., C.C. Fulton, P.J. Hartlieb, R.F. Davis, B.J. Rodriguez, B.J. Shields, and R.J. Nemanich, *In situcleaning and characterization of oxygen- and zinc-terminated,n-type, ZnO {0001} surfaces.* Journal of Applied Physics, 2004. **95**(10): p. 5856-5864.

Brillson, L.J., *Transition in Schottky Barrier Formation with Chemical Reactivity.* Physical Review Letters, 1978. **40**(4): p. 260-263.

Brillson, L.J., H.L. Mosbacker, M.J. Hetzer, Y. Strzhemechny, G.H. Jessen, D.C. Look, G. Cantwell, J. Zhang, and J.J. Song, *Dominant effect of near-interface native point defects on ZnO Schottky barriers.* Applied Physics Letters, 2007. **90**(10): p. 102116.

Kohan, A.F., G. Ceder, D. Morgan, and C.G. Van de Walle, *First-principles study of native point defects in ZnO.* Physical Review B, 2000. **61**(22): p. 15019-15027.

Allen, M.W., S.M. Durbin, and J.B. Metson, *Silver oxide Schottky contacts on n-type ZnO.* Applied Physics Letters, 2007. **91**(5): p. 053512.

Dong, Y., Z.Q. Fang, D.C. Look, G. Cantwell, J. Zhang, J.J. Song, and L.J. Brillson, *Zn- and O-face polarity effects at ZnO surfaces and metal interfaces.* Applied Physics Letters, 2008. **93**(7): p. 072111.

Tsao, J.Y., S. Chowdhury, M.A. Hollis, D. Jena, N.M. Johnson, K.A. Jones, R.J. Kaplar, S. Rajan, C.G. Van de Walle, E. Bellotti, C.L. Chua, R. Collazo, M.E. Coltrin, J.A. Cooper, K.R. Evans, S. Graham, T.A. Grotjohn, E.R. Heller, M. Higashiwaki, M.S. Islam, P.W. Juodawlkis, M.A. Khan, A.D. Koehler, J.H. Leach, U.K. Mishra, R.J. Nemanich, R.C.N. Pilawa-Podgurski, J.B. Shealy, Z. Sitar, M.J. Tadjer, A.F. Witulski, M. Wraback, and J.A. Simmons, *Ultrawide-Bandgap Semiconductors: Research Opportunities and Challenges.* Advanced Electronic Materials, 2018. **4**(1): p. 1600501.

Kato, H., W. Futako, S. Yamasaki, and H. Okushi, *Homoepitaxial growth and characterization of phosphorus-doped diamond using tertiarybutylphosphine as a doping source.* Diamond and Related Materials, 2004. **13**(11-12): p. 2117-2120.

Koizumi, S., M. Kamo, Y. Sato, H. Ozaki, and T. Inuzuka, *Growth and characterization of phosphorous doped {111} homoepitaxial diamond thin films.* Applied Physics Letters, 1997. **71**(8): p. 1065-1067.

Koeck, F.A.M. and R.J. Nemanich, *Advances in Thermionic Energy Conversion through Single-Crystal n-Type Diamond.* Frontiers in Mechanical Engineering, 2017. **3**.

Kono, S., T. Nohara, S. Abe, H. Kodama, K. Suzuki, S. Koizumi, T. Abukawa, and A. Sawabe, *Electron Spectroscopic Determination of Electronic Structures of Phosphorus-Doped n-Type Heteroepitaxial Diamond (001) Surface and Junction.* Japanese Journal of Applied Physics, 2012. **51**: p. 090109.

Suzuki, M., S. Koizumi, M. Katagiri, T. Ono, N. Sakuma, H. Yoshida, T. Sakai, and S. Uchikoga, *Electrical characteristics of n-type diamond Schottky diodes and metal/diamond interfaces.* physica status solidi (a), 2006. **203**(12): p. 3128-3135.

Kawashima, H., H. Kato, M. Ogura, D. Takeuchi, T. Makino, and S. Yamasaki, *Desorption time of phosphorus during MPCVD growth of n-type (001) diamond.* Diamond and Related Materials, 2016. **64**: p. 208-212.

Ogura, M., H. Kato, T. Makino, H. Okushi, and S. Yamasaki, *Misorientation-angle dependence of boron incorporation into (001)-oriented chemical-vapor-deposited (CVD) diamond.* Journal of Crystal Growth, 2011. **317**(1): p. 60-63.

Pinault-Thaury, M.A., T. Tillocher, D. Kobor, N. Habka, F. Jomard, J. Chevallier, and J. Barjon, *Phosphorus donor incorporation in (100) homoepitaxial diamond: Role of the lateral growth.* Journal of Crystal Growth, 2011. **335**(1): p. 31-36.

Pinault-Thaury, M.A., B. Berini, I. Stenger, E. Chikoidze, A. Lusson, F. Jomard, J. Chevallier, and J. Barjon, *High fraction of substitutional phosphorus in a (100) diamond epilayer with low surface roughness.* Applied Physics Letters, 2012. **100**(19): p. 192109.

Nemanich, R.J., P.K. Baumann, M.C. Benjamin, O.H. Nam, A.T. Sowers, B.L. Ward, H. Ade, and R.F. Davis, *Electron emission properties of crystalline diamond and III-nitride surfaces.* Applied Surface Science, 1998. **130-132**: p. 694-703.

Yang, Y., F.A. Koeck, M. Dutta, X. Wang, S. Chowdhury, and R.J. Nemanich, *Al_2O_3 dielectric layers on H-terminated diamond: Controlling surface conductivity.* Journal of Applied Physics, 2017. **122**(15): p. 155304.

Maier, F., M. Riedel, B. Mantel, J. Ristein, and L. Ley, *Origin of Surface Conductivity in Diamond.* Physical Review Letters, 2000. **85**(16): p. 3472-3475.

Takeuchi, D., M. Riedel, J. Ristein, and L. Ley, *Surface band bending and surface conductivity of hydrogenated diamond.* Physical Review B, 2003. **68**(4).

Bhagavantam, S. and D.A.A.S. Narayana Rao, *Dielectric Constant of Diamond.* Nature, 1948. **161**(4097): p. 729-729.

Yamada, T., T. Masuzawa, H. Mimura, and K. Okano, *Electron emission from conduction band of heavily phosphorus doped diamond negative electron affinity surface.* Journal of Physics D: Applied Physics, 2016. **49**(4): p. 045102.

Graupner, R., M. Hollering, A. Ziegler, J. Ristein, L. Ley, and A. Stampfl, *Dispersions of surface states on diamond (100) and (111)*. Physical Review B, 1997. 55(16): p. 10841-10847.

Koeck, F.A.M., R.J. Nemanich, A. Lazea, and K. Haenen, *Thermionic electron emission from low work-function phosphorus doped diamond films*. Diamond and Related Materials, 2009. 18(5-8): p. 789-791.